TRANSACTIONS OF THE INSTITUTE OF MEASUREMENT & CONTROL

Article

Transactions of the Institute of Measurement and Control
2020, Vol. 42(16) 3091–3109

DOI: 10.1177/0142331220940427
journals.sagepub.com/home/tim
SAGE

Speed-adaptive dynamic surface attitude control for a satellite with moving masses under input constraints

Yuandong Hu, Zhengliang Lu and Wenhe Liao

Abstract

This paper investigates an attitude control technique for a low Earth orbit nanosatellite with moving masses based on the active use of aerodynamic forces. A speed-adaptive dynamic surface control scheme is designed to comprehensively solve the practical problems of aerodynamic model error, the dynamic effect of movement, stroke limitation, and slow convergence. Multiple constraints are imposed on the inputs to reduce the fast-varying dynamic effect of the masses to be negligible. Other slow-varying disturbances are precisely estimated by a nonlinear observer. In particular, to resolve the contradiction between the overshoot and the attitude convergence speed, a novel adaptive law is designed based on the smooth hyperbolic tangent function to adjust the convergence parameter within the given boundary. Moreover, considering the actual physical limitation, hard constraints are imposed on two actuators. Finally, by using the Lyapunov approach, it is proven that, despite uncertain dynamics, unknown disturbances and input constraints, the attitude error can be adjusted to be arbitrarily small by choosing the proper parameters. A semi-physical simulation platform is built to verify the feasibility of the moving mass actuator and the effectiveness and robustness of the proposed control scheme.

Keywords

Attitude control, dynamic surface control, input constraints, adaptive law, disturbance observer, semi-physical simulation

Introduction

For LEO (low Earth orbit) nanosatellites, the traditional attitude actuators consume too much energy and may lose control ability due to their high aero-to-inertia ratio and the presence of strong aerodynamic forces (Ye et al., 2018; Zhang et al., 2019). Moving mass actuators, which can actively use the aerodynamic forces as attitude control input, have been proposed as a substitute to traditional attitude control actuators (Chesi, 2015). However, the problems in practical application, i.e. aerodynamic model error, the dynamic effect of movement, stroke limitation, and slow convergence, always exist and are inevitable (Edwards et al., 1974; Guo and Zhao, 2013; Kumar and Zou, 2010).

In fact, the interaction forces between the body and moving masses are capable of directly controlling the attitude (Atkins and Henderson, 2012; Childs, 1971). But this method is not valid for LEO nanosatellites with strong external forces. By modifying the position vector of the spacecraft's center of pressure with respect to the center of mass, moving mass actuators can actively change the external torque vector to control the attitude (Firuzi and Gong, 2018; Petsopoulos et al., 1996; Wie and Murphy, 2007). In LEO, a double symmetry moving mass system was designed to triaxially stabilize the 2U CubeSat (Lu, 2017), but the system was underactuated, as the aerodynamic torque was perpendicular to the relative flow vector. To avoid an underactuated system, Chesi (2015) first proposed to complement the moving mass system with one momentum wheel or a three-axis magnetorquer. The control law can be designed for the three-dimensional ideal control torque, and the torque is then allocated to two actuators. This method greatly decreases the residual oscillation error due to underactuation typically associated with the magnetic controlled attitude of nanosatellites in the presence of residual aerodynamic torque (Chesi et al., 2014; Psiaki, 2004; Lovera et al., 2002), and enables a higher pointing accuracy for LEO nanosatellites. However, Chesi et al. only demonstrated the conceptual feasibility of this method, and ignored the problems in practical application. The error sources of the aerodynamic model were analyzed and the quaternion feedback control law was designed considering the uncertainty of the aerodynamic force (Polat et al., 2016; Virgili-Llop et al., 2016). Lu and Zhang (2016) pointed out that additional torques are related to the velocity and acceleration of masses; this means that the dynamic effect of the movement of masses can be significantly reduced by imposing constraints on the input of actuators. Moreover, to avoid exceeding the stroke of the moving mass actuator, previous research has drastically reduced the gain of the control law (Hill, 2017) or used a

School of Mechanical Engineering, Nanjing University of Science and Technology, China

Corresponding author:
Zhengliang Lu, School of Mechanical Engineering, Nanjing University of Science and Technology, No. 200 Xiaolingwei Street, Xuanwu District, Nanjing, Jiangsu 210094, China.
Email: 112010115@njust.edu.cn

saturation function on the input of actuators (Menon et al., 2004), which might lead the control law to converge for too long, or even to not converge.

Unfortunately, no previous research has comprehensively considered the problems in the practical application of the moving mass actuator, including aerodynamic model error, the dynamic effect of movement, stroke limitation, and slow convergence. Such a system can be summarized as a system subject to complex disturbances and actuator constraints, and some advanced control algorithms have been studied in previous research (Akella et al., 2005; Xia et al., 2019; Yu and Xie, 2019). The constrained backstepping technique was applied to derive a robust control law for spacecraft under input magnitude and rate saturations (Zou et al., 2016). However, this technique requires the boundary information of the disturbance and also suffers from the "explosion of terms" problem. Thereafter, the dynamic surface control technique was incorporated into the traditional backstepping design to circumvent the "explosion of terms" problem (Gao et al., 2016), but it was only applicable to a class of SISO nonlinear systems. In the work by Zhou et al. (2017), the precise estimation of disturbance was achieved based on the observer-based constrained dynamic surface algorithm. However, as the actual control torque is small, the convergence speed should be considered in the algorithm design to attain better performance. Moreover, for a satellite with two actuators, hard constraints caused by physical limits must be imposed on each actuator, rather than the ideal resultant torque.

This paper extends the previous dynamic surface attitude control algorithm by adding a speed-adaptive law and a disturbance observer. The algorithm is designed for a LEO nanosatellite with moving masses to comprehensively solve the practical problems of aerodynamic model error, the dynamic effect of movement, stroke limitation, and slow convergence. Based on the disturbance observer, first-order filters, and adaptive laws, the backstepping control algorithm can smoothly and accurately drive the satellite to maneuver a large angle. Moreover, a semi-physical simulation platform is built for two actuators.

Compared with the preceding studies, the contributions of this approach are summarized as follows:

(1) Actual physical limits of two actuators are considered in the control algorithm. Hard constraints are imposed on the position of each mass and the magnetic moment generated by the magnetorquer;
(2) Multiple constraints are imposed on the inputs to reduce the fast-varying dynamic effect of the masses to be negligible. Other slow-varying disturbances are precisely estimated by a nonlinear observer;
(3) A novel adaptive law is designed for the convergence parameter. The convergence speed can be adaptively adjusted within the given boundary for better control performance.

The remainder of this paper is organized as follows. Equations of motion for a satellite with moving masses and a three-axis magnetorquer are described in Section 2. Section 3 details a speed-adaptive dynamic surface control scheme for an uncertain nonlinear system under actuator input constraints. Section 4 analyzes the method of control torque allocation. Semi-physical simulation results are presented in Section 5, followed by the conclusions in Section 6.

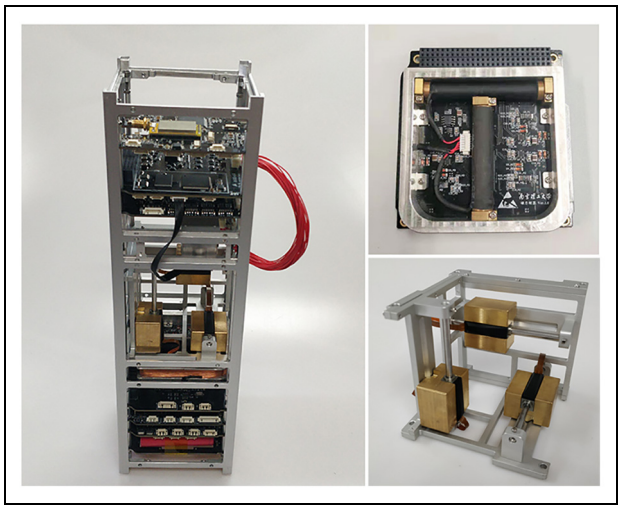

Figure 1. Moving mass actuator and three-axis magnetorquer.

System modeling

Generally, the moving mass actuator contains one, two, or three moving masses. Due to the possible occurrence of the direction of one moving mass being parallel to the aerodynamic force, three moving masses along three different axes are needed to ensure that the center of mass (CoM) can be adjusted in all directions. As the exclusive use of moving masses would lead to an underactuated system, a three-axis magnetorquer is used to complement the moving mass system for full three-dimensional ideal resultant torque. The control law is first designed for the three-dimensional ideal control torque, and the torque is then allocated to two actuators with a control allocation algorithm.

As shown in Figure 1, a prototype design of a moving mass mechanism was made for practical application. There are three moving masses, and each mass moves only along a straight line. The LM0830-040-01 series linear DC-servomotors from FAULHABER were selected for actuating the moving masses. The three-axis magnetorquer was completely designed and manufactured by Nanjing University of Science and Technology. Both the actuators meet the standards of CubeSat. A 3U CubeSat with these two actuators was assembled.

Attitude dynamics of a satellite with moving masses

The satellite was modeled as a rigid body with n moving masses and a three-axis magnetorquer. The following two Cartesian coordinate systems are here defined: an inertial coordinate system $O_I X_I Y_I Z_I$ and a body-fixed coordinate system $O_B X_B Y_B Z_B$.

Figure 2 illustrates the pertinent variables required to derive the equations of motion. The resultant external force

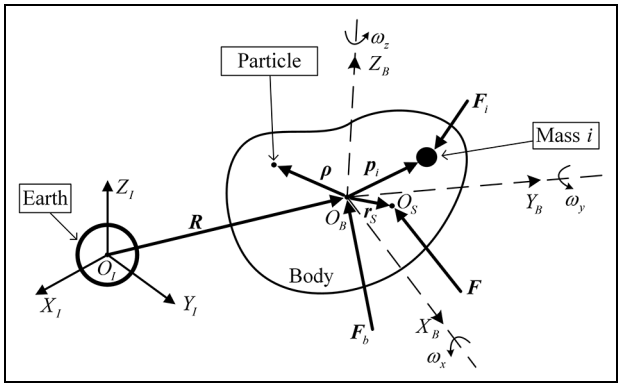

Figure 2. Force diagram of the satellite system.

applied to the system is $\boldsymbol{F}$, and $\boldsymbol{F}_b$ is the resultant external force applied to the rigid body (without moving masses). The force $\boldsymbol{F}_i$ is the net force acting on mass i. The force $\boldsymbol{G}$ is the gravity of the system and $\boldsymbol{F}_e$ is the environmental force applied to the system except $\boldsymbol{G}$. The vector $\boldsymbol{R}$ locates O_B in the $O_IX_IY_IZ_I$ system, the vector $\boldsymbol{p}_i$ locates the mass m_i in the $O_BX_BY_BZ_B$ system, and the vector $\boldsymbol{\rho}$ locates any particle in the $O_BX_BY_BZ_B$ system. The angular velocity vector of the $O_BX_BY_BZ_B$ system is identified by $\boldsymbol{\omega}$.

In this paper, to derive the dynamic equations, the following reasonable assumptions are needed:

Assumption 1: Each moving mass is considered as a point mass due to its high density and small size.

Assumption 2: The satellite is in a circular LEO such that the gravitational forces and the inertial forces due to radial acceleration are in equilibrium.

From Newtonian mechanics, the basic defining equations for the system can be stated as

$$\boldsymbol{F}_b = \int_M \left(\hat{\hat{\boldsymbol{R}}} + \hat{\hat{\boldsymbol{\rho}}}\right) dm \tag{1}$$

$$\boldsymbol{F}_i = m_i\left(\hat{\hat{\boldsymbol{R}}} + \hat{\hat{\boldsymbol{p}}}_i\right) \tag{2}$$

$$\begin{aligned}\boldsymbol{F} = \boldsymbol{G} + \boldsymbol{F}_e &= \boldsymbol{F}_b + \sum_{i=1}^{n} \boldsymbol{F}_i \\ &= \int_M \left(\hat{\hat{\boldsymbol{R}}} + \hat{\hat{\boldsymbol{\rho}}}\right) dm + \sum_{i=1}^{n} m_i\left(\hat{\hat{\boldsymbol{R}}} + \hat{\hat{\boldsymbol{p}}}_i\right)\end{aligned} \tag{3}$$

where M and m_i are the masses of the rigid body and mass i, respectively, and the operation $\hat{\hat{\boldsymbol{v}}}$ implies the second derivative with respect to the $O_IX_IY_IZ_I$ system.

From the vector differentiation rule between coordinate systems, $\hat{\hat{\boldsymbol{p}}}_i$ and $\hat{\hat{\boldsymbol{\rho}}}$ can be expressed as

$$\hat{\hat{\boldsymbol{p}}}_i = \ddot{\boldsymbol{p}}_i + 2\boldsymbol{\omega}\times\dot{\boldsymbol{p}}_i + \dot{\boldsymbol{\omega}}\times\boldsymbol{p}_i + \boldsymbol{\omega}\times(\boldsymbol{\omega}\times\boldsymbol{p}_i) \tag{4}$$

$$\hat{\hat{\boldsymbol{\rho}}} = \dot{\boldsymbol{\omega}}\times\boldsymbol{\rho} + \boldsymbol{\omega}\times(\boldsymbol{\omega}\times\boldsymbol{\rho}) \tag{5}$$

where operations $\dot{\boldsymbol{v}}$ and $\ddot{\boldsymbol{v}}$ imply the first derivative and the second derivative with respect to the $O_BX_BY_BZ_B$ system.

Note that the origin of the $O_BX_BY_BZ_B$ system is defined to coincide with the CoM of the rigid body; hence, $\int_M \boldsymbol{\rho}\, dm = 0$. According to assumption 2, the gravity $\boldsymbol{G}$ can be written as

$$\boldsymbol{G} = \left(M + \sum_{i=1}^{n} m_i\right)\hat{\hat{\boldsymbol{R}}} \tag{6}$$

where $\hat{\hat{\boldsymbol{R}}}$ implies the gravity acceleration of the satellite.

Substitution from (5) and (6) into (3) yields

$$\boldsymbol{F}_e = \left(M + \sum_{i=1}^{n} m_i\right)\delta\hat{\hat{\boldsymbol{R}}} + \sum_{i=1}^{n} m_i\hat{\hat{\boldsymbol{p}}}_i \tag{7}$$

$$\delta\hat{\hat{\boldsymbol{R}}} = \frac{\boldsymbol{F}_e - \sum_{i=1}^{n} m_i\hat{\hat{\boldsymbol{p}}}_i}{M + \sum_{i=1}^{n} m_i} \tag{8}$$

where $\delta\hat{\hat{\boldsymbol{R}}} = \hat{\hat{\boldsymbol{R}}} - \hat{\hat{\boldsymbol{R}}}$ refers to the acceleration of the body due to the mass motion.

The mass i is subjected to its gravity and the force $\boldsymbol{f}_i$ applied by the body. The force $\boldsymbol{f}_i$ can be expressed as

$$\boldsymbol{f}_i = m_i\left(\delta\hat{\hat{\boldsymbol{R}}} + \hat{\hat{\boldsymbol{p}}}_i\right) \tag{9}$$

Hence, the torque that the masses apply to the rigid body is given by

$$\boldsymbol{T}_m = -\sum_{i=1}^{n} \boldsymbol{p}_i\times\boldsymbol{f}_i \tag{10}$$

The rigid body is subjected to the following three torques: the control torque $\boldsymbol{T}_B$ generated by the magnetorquer, the moment of environmental force relative to the CoM of the body $\boldsymbol{T}_e$, and the torque $\boldsymbol{T}_m$. The inertia matrix of the body is $\boldsymbol{J}_B$. Therefore, the dynamic equation of the body is given by

$$\boldsymbol{J}_B\dot{\boldsymbol{\omega}} + \boldsymbol{\omega}\times\boldsymbol{J}_B\boldsymbol{\omega} = \boldsymbol{T}_B + \boldsymbol{T}_e + \boldsymbol{T}_m \tag{11}$$

where $\boldsymbol{T}_B = \boldsymbol{m}_B\times\boldsymbol{B}$, $\boldsymbol{m}_B = [m_{B1}, m_{B2}, m_{B3}]^{\mathrm{T}}$ is the magnetic moment generated by the magnetorquer, and $\boldsymbol{B}$ is the geomagnetic vector expressed in the $O_BX_BY_BZ_B$ system.

Substitution from (8) and (9) into (10) yields

$$\boldsymbol{T}_m = -\boldsymbol{r}_s\times\boldsymbol{F}_e + \left[\boldsymbol{r}_s\times\sum_{i=1}^{n} m_i\hat{\hat{\boldsymbol{p}}}_i - \sum_{i=1}^{n}\left(m_i\boldsymbol{p}_i\times\hat{\hat{\boldsymbol{p}}}_i\right)\right] \tag{12}$$

where the vector $\boldsymbol{r}_s$ locates the CoM of the system O_S in the $O_BX_BY_BZ_B$ system and can be written as

$$\boldsymbol{r}_s = \frac{\sum_{i=1}^{n} m_i\boldsymbol{p}_i}{M + \sum_{i=1}^{n} m_i} \tag{13}$$

Substitution from (4) into the second term on the right side of (12) yields

$$\boldsymbol{r}_s\times\sum_{i=1}^{n} m_i\hat{\hat{\boldsymbol{p}}}_i - \sum_{i=1}^{n}\left(m_i\boldsymbol{p}_i\times\hat{\hat{\boldsymbol{p}}}_i\right) = \boldsymbol{M}_a + \boldsymbol{M}_c + \boldsymbol{M}_g - \boldsymbol{J}_M\dot{\boldsymbol{\omega}} \tag{14}$$

where

$$\begin{cases} \boldsymbol{J}_M = [\boldsymbol{r}_s]^\times \left[\sum_{i=1}^{n} m_i \boldsymbol{p}_i\right]^\times - \sum_{i=1}^{n} m_i [\boldsymbol{p}_i]^\times [\boldsymbol{p}_i]^\times \\ \boldsymbol{M}_{xt} = \boldsymbol{M}_a + \boldsymbol{M}_c + \boldsymbol{M}_g \\ \boldsymbol{M}_a = \boldsymbol{r}_s \times \sum_{i=1}^{n} m_i \ddot{\boldsymbol{p}}_i - \sum_{i=1}^{n} m_i \boldsymbol{p}_i \times \ddot{\boldsymbol{p}}_i \\ \boldsymbol{M}_c = \boldsymbol{r}_s \times \left(2\boldsymbol{\omega} \times \sum_{i=1}^{n} m_i \dot{\boldsymbol{p}}_i\right) - \sum_{i=1}^{n} 2 m_i \boldsymbol{p}_i \times (\boldsymbol{\omega} \times \dot{\boldsymbol{p}}_i) \\ \boldsymbol{M}_g = \boldsymbol{r}_s \times \left[\boldsymbol{\omega} \times \left(\boldsymbol{\omega} \times \sum_{i=1}^{n} m_i \boldsymbol{p}_i\right)\right] - \sum_{i=1}^{n} m_i \boldsymbol{p}_i \times [\boldsymbol{\omega} \times (\boldsymbol{\omega} \times \boldsymbol{p}_i)] \end{cases} \tag{15}$$

in which $\boldsymbol{J}_M$ is the additional moment of inertia related to the position of the masses, $\boldsymbol{M}_a$ is the additional inertial torque related to acceleration $\ddot{\boldsymbol{p}}_i$, $\boldsymbol{M}_c$ is the additional Coriolis torque related to velocity $\dot{\boldsymbol{p}}_i$, $\boldsymbol{M}_g$ is the additional gyroscopic torque related to position $\boldsymbol{p}_i$, and $\boldsymbol{M}_{xt}$ is the total additional torque caused by the movement.

By combining (11), (12), and (14), the complete dynamic equation of the satellite with n moving masses and a three-axis magnetorquer can be written as

$$(\boldsymbol{J}_B + \boldsymbol{J}_M)\dot{\boldsymbol{\omega}} + \boldsymbol{\omega} \times \boldsymbol{J}_B \boldsymbol{\omega} = \boldsymbol{T}_e + \boldsymbol{T}_B - \boldsymbol{r}_s \times \boldsymbol{F}_e + \boldsymbol{M}_{xt} \tag{16}$$

Remark 1: The atmospheric environment is variable and poorly predictable, and spacecraft aerodynamics are not particularly well understood (Virgili-Llop et al., 2019). In LEO, the environmental force $\boldsymbol{F}_e$ can be simplified to be the ideal aerodynamic force $\boldsymbol{F}_{aero}$ with unknown errors in magnitude and direction. The ideal aerodynamic model can be used to calculate $\boldsymbol{F}_{aero}$ (Chesi et al., 2017). The uncertainty of the atmospheric environment will lead to control torque errors and ultimately affect the attitude control.

Error kinematics and error dynamics

To describe the attitude, two other coordinate systems are here defined: an orbit coordinate system $O_O X_O Y_O Z_O$ and a desired coordinate system $O_D X_D Y_D Z_D$. The angular velocity of the spacecraft with respect to the $O_O X_O Y_O Z_O$ system can be expressed as

$$\boldsymbol{\omega}_{bo} = \boldsymbol{\omega} - \boldsymbol{A}_{bo}\boldsymbol{\omega}_{oi} \tag{17}$$

where $\boldsymbol{A}_{bo}$ denotes the direction cosine matrix from the $O_O X_O Y_O Z_O$ system to the $O_B X_B Y_B Z_B$ system, and $\boldsymbol{\omega}_{oi}$ represents the angular velocity of the $O_O X_O Y_O Z_O$ system with respect to the $O_I X_I Y_I Z_I$ system expressed in the $O_O X_O Y_O Z_O$ system.

After taking the time derivative of (17) and using the fact that $\dot{\boldsymbol{A}}_{bo} = -\boldsymbol{\omega}_{bo} \times \boldsymbol{A}_{bo}$ and $\dot{\boldsymbol{\omega}}_{oi} = 0$, the following is obtained

$$\dot{\boldsymbol{\omega}}_{bo} = \dot{\boldsymbol{\omega}} + \boldsymbol{\omega}_{bo} \times \boldsymbol{A}_{bo}\boldsymbol{\omega}_{oi} \tag{18}$$

By substituting (18) into (16), the dynamic equation relative to the $O_O X_O Y_O Z_O$ system can be written as

$$\begin{aligned}(\boldsymbol{J}_B + \boldsymbol{J}_M)\dot{\boldsymbol{\omega}}_{bo} = &-\boldsymbol{\omega} \times \boldsymbol{J}_B \boldsymbol{\omega} + (\boldsymbol{J}_B + \boldsymbol{J}_M)(\boldsymbol{\omega}_{bo} \times \boldsymbol{A}_{bo}\boldsymbol{\omega}_{oi}) \\ &+ \boldsymbol{T}_e + \boldsymbol{T}_B - \boldsymbol{r}_s \times \boldsymbol{F}_e + \boldsymbol{M}_{xt}\end{aligned} \tag{19}$$

The desired angular velocity $\boldsymbol{\omega}_d$ is defined as the angular velocity of the $O_D X_D Y_D Z_D$ system with respect to the $O_O X_O Y_O Z_O$ system expressed in the $O_D X_D Y_D Z_D$ system. The error angular velocity $\boldsymbol{\omega}_e$ denotes the angular velocity of the $O_B X_B Y_B Z_B$ system with respect to the $O_D X_D Y_D Z_D$ system expressed in the $O_B X_B Y_B Z_B$ system, and is given by

$$\boldsymbol{\omega}_e = \boldsymbol{\omega}_{bo} - \boldsymbol{A}_e \boldsymbol{\omega}_d \tag{20}$$

where $\boldsymbol{A}_e$ denotes the direction cosine matrix from the $O_D X_D Y_D Z_D$ system to the $O_B X_B Y_B Z_B$ system.

After taking the time derivative of (20) and using the fact that $\dot{\boldsymbol{A}}_e = -\boldsymbol{\omega}_e \times \boldsymbol{A}_e$, the following is obtained

$$\dot{\boldsymbol{\omega}}_e = \dot{\boldsymbol{\omega}}_{bo} + \boldsymbol{\omega}_e \times \boldsymbol{A}_e \boldsymbol{\omega}_d - \boldsymbol{A}_e \dot{\boldsymbol{\omega}}_d \tag{21}$$

By substituting (21) into (19), the error dynamic equation can be established as

$$\begin{aligned}(\boldsymbol{J}_B + \boldsymbol{J}_M)\dot{\boldsymbol{\omega}}_e = &-\boldsymbol{\omega} \times \boldsymbol{J}_B \boldsymbol{\omega} + \boldsymbol{T}_e + \boldsymbol{T}_B - \boldsymbol{r}_s \times \boldsymbol{F}_e + \boldsymbol{M}_{xt} \\ &+ (\boldsymbol{J}_B + \boldsymbol{J}_M)(\boldsymbol{\omega}_{bo} \times \boldsymbol{A}_{bo}\boldsymbol{\omega}_{oi} + \boldsymbol{\omega}_e \times \boldsymbol{A}_e \boldsymbol{\omega}_d - \boldsymbol{A}_e \dot{\boldsymbol{\omega}}_d)\end{aligned} \tag{22}$$

The modified Rodrigues (MRS) parameter $\boldsymbol{\sigma}_e$ is used to represent the attitude mapping from the $O_D X_D Y_D Z_D$ system to the $O_B X_B Y_B Z_B$ system. The error kinematic equation based on MRS can be expressed as

$$\dot{\boldsymbol{\sigma}}_e = \boldsymbol{G}(\boldsymbol{\sigma}_e)\boldsymbol{\omega}_e \tag{23}$$

where $\boldsymbol{G}(\boldsymbol{\sigma}_e)$ satisfies

$$\boldsymbol{G}(\boldsymbol{\sigma}_e) = \frac{1}{2}\left(\boldsymbol{I}_{3\times 3} + [\boldsymbol{\sigma}_e]^\times + \boldsymbol{\sigma}_e \boldsymbol{\sigma}_e{}^T - \frac{1 + \boldsymbol{\sigma}_e{}^{\mathrm{T}}\boldsymbol{\sigma}_e}{2}\boldsymbol{I}_{3\times 3}\right) \tag{24}$$

with $\boldsymbol{I}_{3\times 3} \in \boldsymbol{R}^{3\times 3}$ denoting the identity matrix and $[\cdot]^\times$ representing the cross-product operator (Zou et al., 2011).

The corresponding direction cosine matrix is given by

$$\boldsymbol{A}_e = \boldsymbol{I}_{3\times 3} - \frac{4\left(1 - \boldsymbol{\sigma}_e{}^{\mathrm{T}}\boldsymbol{\sigma}_e\right)}{\left(1 + \boldsymbol{\sigma}_e{}^{\mathrm{T}}\boldsymbol{\sigma}_e\right)^2}[\boldsymbol{\sigma}_e]^\times + \frac{8}{\left(1 + \boldsymbol{\sigma}_e{}^{\mathrm{T}}\boldsymbol{\sigma}_e\right)^2}[\boldsymbol{\sigma}_e]^{\times 2} \tag{25}$$

Controller design

In this paper, the resultant torque generated by two actuators is considered as a three-dimensional ideal control torque. A speed-adaptive dynamic surface control algorithm is designed for this resultant torque. Thereafter, the control torque is allocated to two actuators. The stability of the designed controller is proven by the Lyapunov principle.

The ideal control torque is given by

$$\boldsymbol{u}_t = \boldsymbol{T}_B - \boldsymbol{r}_s \times \boldsymbol{F}_e \tag{26}$$

The following sources of the disturbances are considered:

(1) $\Delta \boldsymbol{r}_s$: the unknown deviation of the CoM position of the body;
(2) $\boldsymbol{T}_e$: the unknown moment of environmental force relative to the CoM of the body;
(3) $\boldsymbol{M}_{xt}$: the additional torque caused by the motion of moving masses;
(4) $\Delta \boldsymbol{F}_{aero}$: the unknown error of the aerodynamic force in magnitude and direction;
(5) $\Delta \boldsymbol{m}_B$: the unknown remanent magnetic moment of the satellite system;
(6) $\Delta \boldsymbol{d}$: some other unknown disturbances.

It is to be noted that $\Delta \boldsymbol{r}_s$, $\boldsymbol{T}_e$, and $\Delta \boldsymbol{m}_B$ are parameter uncertainties of the system. The rates of disturbance torque caused by these sources are related to the angular velocity. In fact, as long as the observer is updated fast enough, these disturbances can be considered to be stable. The rate of $\Delta \boldsymbol{F}_{aero}$ is related to the rate of atmospheric change, which is very slow.

In addition, equation (15) implies that the dynamic effect $\boldsymbol{M}_{xt}$ is related to the position, speed and acceleration of each mass and is fast-varying. To reduce this fast-varying disturbance, multiple constraints can be imposed on the movement of each mass. Although constraints can only be imposed on the ideal control torque rather than actuators, they can greatly influence the motion of the moving masses. Thus, the position, speed, and acceleration of each mass can be indirectly limited to a certain extent. Moreover, other disturbances are all related to the change of the environment and can be considered as slow-varying.

An auxiliary error (Xia et al., 2011) is defined

$$\boldsymbol{x} = k\boldsymbol{\sigma}_e + \boldsymbol{\omega}_e \tag{27}$$

where the parameter k is time-varying, but $k > 0$ is required to ensure the convergence of the errors $\boldsymbol{\sigma}_e$ and $\boldsymbol{\omega}_e$.

Substitution from (23), (26), and (27) into (22) yields

$$\begin{aligned}(\boldsymbol{J}_B + \boldsymbol{J}_M)\dot{\boldsymbol{x}} = &- \boldsymbol{\omega} \times \boldsymbol{J}_B\boldsymbol{\omega} + (\boldsymbol{J}_B + \boldsymbol{J}_M)(\boldsymbol{\omega}_{bo} \times \boldsymbol{A}_{bo}\boldsymbol{\omega}_{oi}) \\ &+ (\boldsymbol{J}_B + \boldsymbol{J}_M)(\boldsymbol{\omega}_e \times \boldsymbol{A}_e\boldsymbol{\omega}_d - \boldsymbol{A}_e\dot{\boldsymbol{\omega}}_d + k\dot{\boldsymbol{\sigma}}_e) \\ &+ \boldsymbol{u}_t + \boldsymbol{M}_{xt} + \Delta \boldsymbol{m}_B \times \boldsymbol{B} + \Delta \boldsymbol{d} \\ &+ [-\boldsymbol{r}_s \times \Delta \boldsymbol{F}_{aero} - \Delta \boldsymbol{r}_s \times (\boldsymbol{F}_{aero} + \Delta \boldsymbol{F}_{aero})]\end{aligned} \tag{28}$$

where $\Delta \boldsymbol{m}_B \times \boldsymbol{B}$ is the remanent magnetic disturbance torque and $-\boldsymbol{r}_s \times \Delta \boldsymbol{F}_{aero} - \Delta \boldsymbol{r}_s \times (\boldsymbol{F}_{aero} + \Delta \boldsymbol{F}_{aero})$ is the disturbance torque caused by $\Delta \boldsymbol{F}_{aero}$ and $\Delta \boldsymbol{r}_s$.

Lemma 1: (Xia et al., 2011) Consider the satellite system (22) and (23). Then, for any $\boldsymbol{x}(t)$ satisfying $\lim_{t\to\infty}\|\boldsymbol{x}(t)\| = 0$, it follows that $\lim_{t\to\infty}\|\boldsymbol{\sigma}_e\| = 0$ and $\lim_{t\to\infty}\|\boldsymbol{\omega}_e\| = 0$.

The uncertainties and disturbances are lumped together as the total vector of disturbance. Applying simple algebraic transformations to (28), the simplified model can be written as

$$\dot{\boldsymbol{x}} = \boldsymbol{F}_x + \boldsymbol{J}^{-1}\boldsymbol{u}_t + \boldsymbol{d} \tag{29}$$

where $\boldsymbol{J} = \boldsymbol{J}_B + \boldsymbol{J}_M$, and $\boldsymbol{d}$ is the total disturbance. $\boldsymbol{F}_x$ and $\boldsymbol{d}$ are, respectively, given by

$$\begin{cases} \boldsymbol{F}_x = -\boldsymbol{J}^{-1}\boldsymbol{\omega} \times \boldsymbol{J}_B\boldsymbol{\omega} + \boldsymbol{\omega}_{bo} \times \boldsymbol{A}_{bo}\boldsymbol{\omega}_{oi} + \boldsymbol{\omega}_e \times \boldsymbol{A}_e\boldsymbol{\omega}_d - \boldsymbol{A}_e\dot{\boldsymbol{\omega}}_d + k\dot{\boldsymbol{\sigma}}_e \\ \boldsymbol{d} = -\boldsymbol{J}^{-1}[\boldsymbol{r}_s \times \Delta \boldsymbol{F}_{aero} + \Delta \boldsymbol{r}_s \times (\boldsymbol{F}_{aero} + \Delta \boldsymbol{F}_{aero})] + \boldsymbol{J}^{-1}(\Delta \boldsymbol{m}_B \times \boldsymbol{B} + \Delta \boldsymbol{d} + \boldsymbol{M}_{xt}) \end{cases} \tag{30}$$

Nonlinear disturbance observer design

In this subsection, a nonlinear observer is designed to estimate the disturbance, and the following assumptions are needed.

Assumption 3: The attitude of the satellite can be fully measured, which implies that the angular velocity parameters and the modified Rodrigues parameters are available for the nonlinear disturbance observer and the controller design (Luo et al., 2005).

Assumption 4: If the additional torque $\boldsymbol{M}_{xt}$ is much smaller than other disturbances, it can be assumed that the disturbance $\boldsymbol{d}$ varies slowly relative to the observer dynamics, and $\dot{\boldsymbol{d}} = 0$. Thus, this observer does not need prior information about the derivative of the disturbance (Chen et al., 2000).

The vector $\hat{\boldsymbol{d}}$ is defined as the observed value of $\boldsymbol{d}$. The nonlinear disturbance observer is constructed as

$$\begin{cases} \hat{\boldsymbol{d}} = \boldsymbol{z} + \boldsymbol{p}(\boldsymbol{x}) \\ \dot{\boldsymbol{z}} = -\dfrac{\partial \boldsymbol{p}(\boldsymbol{x})}{\partial \boldsymbol{x}}\left(\boldsymbol{F}_x + \boldsymbol{J}^{-1}\boldsymbol{u}_t\right) - \dfrac{\partial \boldsymbol{p}(\boldsymbol{x})}{\partial \boldsymbol{x}}[\boldsymbol{z} + \boldsymbol{p}(\boldsymbol{x})] \end{cases} \tag{31}$$

where $\boldsymbol{p}(\boldsymbol{x})$ is the nonlinear function.

Defining the observer error $\tilde{\boldsymbol{d}} = \boldsymbol{d} - \hat{\boldsymbol{d}}$ and combining it with (31) yields

$$\dot{\tilde{\boldsymbol{d}}} = \dot{\boldsymbol{d}} - \dot{\hat{\boldsymbol{d}}} = -\dot{\hat{\boldsymbol{d}}} = -\dot{\boldsymbol{z}} - \frac{\partial \boldsymbol{p}(\boldsymbol{x})}{\partial \boldsymbol{x}}\dot{\boldsymbol{x}} \tag{32}$$

To prove that the observed value $\hat{\boldsymbol{d}}$ can track the disturbance $\boldsymbol{d}$, a Lyapunov function is designed as

$$\boldsymbol{V} = \frac{1}{2}\tilde{\boldsymbol{d}}^{\mathrm{T}}\tilde{\boldsymbol{d}} > 0 \tag{33}$$

After taking the time derivative of (33) and combining it with (32), the following is obtained

$$\dot{\boldsymbol{V}} = \tilde{\boldsymbol{d}}^{\mathrm{T}}\dot{\tilde{\boldsymbol{d}}} = \tilde{\boldsymbol{d}}^{\mathrm{T}}\left(-\dot{\boldsymbol{z}} - \frac{\partial \boldsymbol{p}(\boldsymbol{x})}{\partial \boldsymbol{x}}\dot{\boldsymbol{x}}\right) \tag{34}$$

Substituting (29) and (31) into (34) yields

$$\begin{aligned}\dot{\boldsymbol{V}} &= \tilde{\boldsymbol{d}}^{\mathrm{T}}\left[\frac{\partial \boldsymbol{p}(\boldsymbol{x})}{\partial \boldsymbol{x}}\left(\boldsymbol{F}_x + \boldsymbol{J}^{-1}\boldsymbol{u}_t\right) + \frac{\partial \boldsymbol{p}(\boldsymbol{x})}{\partial \boldsymbol{x}}\hat{\boldsymbol{d}}\right] \\ &\quad - \tilde{\boldsymbol{d}}^{\mathrm{T}}\frac{\partial \boldsymbol{p}(\boldsymbol{x})}{\partial \boldsymbol{x}}\left(\boldsymbol{F}_x + \boldsymbol{J}^{-1}\boldsymbol{u}_t + \boldsymbol{d}\right) \\ &= \tilde{\boldsymbol{d}}^{\mathrm{T}}\frac{\partial \boldsymbol{p}(\boldsymbol{x})}{\partial \boldsymbol{x}}\left(\hat{\boldsymbol{d}} - \boldsymbol{d}\right) = -\tilde{\boldsymbol{d}}^{\mathrm{T}}\frac{\partial \boldsymbol{p}(\boldsymbol{x})}{\partial \boldsymbol{x}}\tilde{\boldsymbol{d}}\end{aligned} \tag{35}$$

The nonlinear function $\boldsymbol{p}(\boldsymbol{x})$ is defined as (Wang and Wu, 2015)

$$\boldsymbol{p}(\boldsymbol{x}) = \begin{bmatrix}\lambda_1(x_1 + {x_1}^{s_1}/s_1) \\ \lambda_2(x_2 + {x_1}^{s_2}/s_2) \\ \lambda_3(x_3 + {x_1}^{s_3}/s_3)\end{bmatrix} \tag{36}$$

where $\lambda_i > 0$, and $s_i > 0$ is an odd integer ($i = 1, 2, 3$). Taking the partial derivative of $\boldsymbol{p}(\boldsymbol{x})$ with respect to $\boldsymbol{x}$, the following is obtained

$$\frac{\partial \boldsymbol{p}(\boldsymbol{x})}{\partial \boldsymbol{x}} = \begin{bmatrix}\lambda_1(1 + {x_1}^{s_1-1}) & 0 & 0 \\ 0 & \lambda_2(1 + {x_1}^{s_2-1}) & 0 \\ 0 & 0 & \lambda_3(1 + {x_1}^{s_3-1})\end{bmatrix} \tag{37}$$

It is clear that $\partial \boldsymbol{p}(\boldsymbol{x})/\partial \boldsymbol{x}$ is a positive definite matrix, and when $\tilde{\boldsymbol{d}} \neq \boldsymbol{0}$, $\dot{\boldsymbol{V}} < 0$.Therefore, the observer error $\tilde{\boldsymbol{d}}$ converges to the origin. From (31) and (32), the following is obtained

$$\dot{\tilde{\boldsymbol{d}}} = -\frac{\partial \boldsymbol{p}(\boldsymbol{x})}{\partial \boldsymbol{x}}\tilde{\boldsymbol{d}} \tag{38}$$

Lemma 2: (Ioannou and Sun, 1995) For any $\kappa : [0, \infty) \in R$, the solution of the inequality equation $\dot{\kappa} \leqslant -\alpha\kappa + f$, $\forall t \geqslant t_0 \geqslant 0$ is

$$\kappa(t) \leqslant e^{-\alpha(t-t_0)}\kappa(t_0) + \int_{t_0}^{t} e^{-\alpha(t-\tau)}f(\tau)d\tau \tag{39}$$

where α is an arbitrary constant. If $f = 0$ and $\alpha > 0$, it yields $\kappa(t) \leqslant e^{-\alpha(t-t_0)}\kappa(t_0)$ and converges to zero in exponential form.

Thus, the observer is globally asymptotically stable and $\tilde{\boldsymbol{d}}$ converges to zero at an exponential rate. In view of the effective compensation, the controller can provide a fast and accurate response.

Speed-adaptive dynamic surface controller design

In this subsection, the dynamic surface technique is adopted to design the controller, and a novel adaptive law is proposed for better control performance.

Assumption 5: For the observer error $\tilde{\boldsymbol{d}} = [\tilde{d}_1, \tilde{d}_2, \tilde{d}_3]^{\mathrm{T}}$, there exist unknown positive constants d_1^+, d_2^+, and d_3^+ such that $|\tilde{d}_1| \leqslant d_1^+$, $|\tilde{d}_2| \leqslant d_2^+$, and $|\tilde{d}_3| \leqslant d_3^+$ (Zhou et al., 2017).

Two operators for a vector $\boldsymbol{x} \in \boldsymbol{R}^3$ are, respectively, defined as $\mathrm{Tanh}(\boldsymbol{x}) = [\tanh(x_1), \tanh(x_2), \tanh(x_3)]^{\mathrm{T}}$ and $\mathrm{Diag}(\boldsymbol{x}) = \mathrm{diag}(x_1, x_2, x_3)$. Based on the properties of hyperbolic tangent functions, the model subject to input constraints is defined as follows

$$\boldsymbol{u}_t = g(\boldsymbol{v}) = \boldsymbol{u}_M \mathrm{Tanh}\left(\frac{\boldsymbol{v}}{\boldsymbol{u}_M}\right) \tag{40}$$

$$\dot{\boldsymbol{u}}_t = f(\boldsymbol{w}) = \frac{\partial g}{\partial \boldsymbol{v}}\dot{\boldsymbol{v}} = \boldsymbol{v}_M \mathrm{Tanh}\left(\frac{\boldsymbol{w}}{\boldsymbol{v}_M}\right) \tag{41}$$

$$\ddot{\boldsymbol{u}}_t = h(\boldsymbol{q}) = \frac{\partial f}{\partial \boldsymbol{w}}\dot{\boldsymbol{w}} = \boldsymbol{w}_M \mathrm{Tanh}\left(\frac{\boldsymbol{q}}{\boldsymbol{w}_M}\right) \tag{42}$$

where $\boldsymbol{u}_M = [u_{1M}, u_{2M}, u_{3M}]^{\mathrm{T}}$, $\boldsymbol{v}_M = [v_{1M}, v_{2M}, v_{3M}]^{\mathrm{T}}$, and $\boldsymbol{w}_M = [w_{1M}, w_{2M}, w_{3M}]^{\mathrm{T}}$ are the given positive upper bounds of $\boldsymbol{u}_t$, $\dot{\boldsymbol{u}}_t$, and $\ddot{\boldsymbol{u}}_t$, respectively. The vectors $\boldsymbol{v}$, $\boldsymbol{w}$, and $\boldsymbol{q}$ are the auxiliary control signals.

Therefore, it satisfies the constraints on the ideal torque magnitude, its first derivative, and its second derivative, that is, $|u_{it}| \leqslant u_{iM}$, $|\dot{u}_{it}| \leqslant v_{iM}$, and $|\ddot{u}_{it}| \leqslant w_{iM}$ ($i = 1, 2, 3$). For the auxiliary system (42), the control signal to be designed is $\boldsymbol{q}$, but (42) is non-affine in $\boldsymbol{q}$, which is difficult for the development of $\boldsymbol{q}$. To solve this problem, another auxiliary system is constructed (Zou et al., 2016) as

$$\dot{\boldsymbol{q}} = \left(\frac{\partial h}{\partial \boldsymbol{q}}\right)^{-1}\boldsymbol{\mu} = \mathrm{diag}\left(\frac{4}{\left(e^{q1/wM1} + e^{-q1/wM1}\right)^2}, \frac{4}{\left(e^{q2/wM2} + e^{-q2/wM2}\right)^2}, \frac{4}{\left(e^{q3/wM3} + e^{-q3/wM3}\right)^2}\right)\boldsymbol{\mu} \tag{43}$$

where $\boldsymbol{\mu} \in \boldsymbol{R}^3$ is an auxiliary signal to be designed by using the backstepping approach. Moreover, the dynamics of the auxiliary control signals $\boldsymbol{v}$ and $\boldsymbol{w}$ are given by

$$\dot{\boldsymbol{v}} = \left(\frac{\partial g}{\partial \boldsymbol{v}}\right)^{-1} f(\boldsymbol{w}) = \mathrm{diag}\left(\frac{4}{\left(e^{v1/uM1} + e^{-v1/uM1}\right)^2}, \frac{4}{\left(e^{v2/uM2} + e^{-v2/uM2}\right)^2}, \frac{4}{\left(e^{v3/uM3} + e^{-v3/uM3}\right)^2}\right)f(\boldsymbol{w}) \tag{44}$$

$$\dot{\boldsymbol{w}} = \left(\frac{\partial f}{\partial \boldsymbol{w}}\right)^{-1} h(\boldsymbol{q}) = \mathrm{diag}\left(\frac{4}{\left(e^{w1/vM1} + e^{-w1/vM1}\right)^2}, \frac{4}{\left(e^{w2/vM2} + e^{-w2/vM2}\right)^2}, \frac{4}{\left(e^{w3/vM3} + e^{-w3/vM3}\right)^2}\right)h(\boldsymbol{q}) \tag{45}$$

The procedure of the controller design is explained as follows.

Step 1: Design of the virtual controller for $g(\boldsymbol{v})$. An auxiliary error $\boldsymbol{z}_1$ is defined as

$$\boldsymbol{z}_1 = \boldsymbol{c}_e\boldsymbol{x} = \boldsymbol{c}_e(k\boldsymbol{\sigma}_e + \boldsymbol{\omega}_e) \tag{46}$$

where $\boldsymbol{c}_e = \mathrm{diag}(c_{1e}, c_{2e}, c_{3e})$ and $c_{1e}, c_{2e}, c_{3e} > 0$.

Note that the parameter k in (27) affects the overshoot of two actuators and the convergence speed of the control law. The greater the parameter k, the higher the convergence speed, but the undesired overshoot of two actuators will be larger, especially when the attitude error $\boldsymbol{x}$ is large.

To resolve the contradiction between the overshoot and the attitude convergence speed, a novel adaptive law for the parameter k is given by

$$\dot{k} = -\gamma_1\left[(k_u - k_l)\tanh\left(\frac{\boldsymbol{z}_1{}^{\mathrm{T}}\boldsymbol{z}_1}{\varepsilon_1}\right) - k_u + k\right] \tag{47}$$

where k_u and k_l are given positive upper and lower bounds of the parameter k, respectively. The coefficient $\gamma_1 > 0$ is an adaption gain to be determined and $\varepsilon_1 > 0$ is a given constant.

In this adaptive law, the parameter k turns to be small to reduce the overshoot in the case of a large attitude error $\boldsymbol{x}$, and turns to be large to increase the convergence speed in the case of a small attitude error $\boldsymbol{x}$. To avoid k being too large or too small, the smooth hyperbolic tangent function is used to guarantee $k_l \leqslant k \leqslant k_u$. Moreover, the initial value k_0 needs to satisfy $0 < k_l \leqslant k_0 \leqslant k_u$ to ensure that k varies between the upper and lower bounds.

The error $\tilde{k} = k_u - k$ is defined, and the error equation is

$$\dot{\tilde{k}} = \dot{k}_u - \dot{k} = -\dot{k} = \gamma_1\left[(k_u - k_l)\tanh\left(\frac{\boldsymbol{z}_1{}^{\mathrm{T}}\boldsymbol{z}_1}{\varepsilon_1}\right) - k_u + k\right] \tag{48}$$

The vector $\hat{\boldsymbol{d}}^+$ is defined as the estimate of the vector $\boldsymbol{d}^+ = [d_1^+, d_2^+, d_3^+]^{\mathrm{T}}$, and another adaptive law for $\hat{\boldsymbol{d}}^+$ is given by

$$\dot{\hat{\boldsymbol{d}}}^+ = \gamma_2\left[\mathrm{Diag}\left(\mathrm{Tanh}\left(\frac{\boldsymbol{z}_1}{\boldsymbol{\varepsilon}_2}\right)\right)\boldsymbol{c}_e\boldsymbol{z}_1 - \hat{\boldsymbol{d}}^+\right] \tag{49}$$

where $\gamma_2 > 0$ is an adaption gain to be determined, and $\boldsymbol{\varepsilon}_2 = [\varepsilon_{21}, \varepsilon_{22}, \varepsilon_{23}]^{\mathrm{T}}$ ($\varepsilon_{21}, \varepsilon_{22}, \varepsilon_{23} > 0$).

Hence, the dynamic equation for the error $\tilde{\boldsymbol{d}}^+ = \boldsymbol{d}^+ - \hat{\boldsymbol{d}}^+$ is

$$\dot{\tilde{\boldsymbol{d}}}^+ = \dot{\boldsymbol{d}}^+ - \dot{\hat{\boldsymbol{d}}}^+ = -\dot{\hat{\boldsymbol{d}}}^+ = -\gamma_2\left[\mathrm{Diag}\left(\mathrm{Tanh}\left(\frac{\boldsymbol{z}_1}{\boldsymbol{\varepsilon}_2}\right)\right)\boldsymbol{c}_e\boldsymbol{z}_1 - \hat{\boldsymbol{d}}^+\right] \tag{50}$$

The first virtual controller $\boldsymbol{\alpha}_2 = g(\boldsymbol{v}) - \boldsymbol{z}_2$ is defined, and the first Lyapunov function for $\boldsymbol{z}_1$ is designed as

$$V_1 = \frac{1}{2}\boldsymbol{z}_1{}^{\mathrm{T}}\boldsymbol{z}_1 + \frac{1}{2\gamma_1}\tilde{k}^2 + \frac{1}{2\gamma_2}\tilde{\boldsymbol{d}}^{+\mathrm{T}}\tilde{\boldsymbol{d}}^+ \tag{51}$$

After taking the time derivative of (51) and combining (46), (48), and (50), the following is obtained

$$\begin{aligned}\dot{V}_1 &= \boldsymbol{z}_1{}^{\mathrm{T}}\dot{\boldsymbol{z}}_1 + \frac{1}{\gamma_2}\tilde{\boldsymbol{d}}^{+\mathrm{T}}\dot{\tilde{\boldsymbol{d}}}^+ + \frac{1}{\gamma_1}\tilde{k}\dot{\tilde{k}} \\ &= \boldsymbol{z}_1{}^{\mathrm{T}}\boldsymbol{c}_e\left[\boldsymbol{F}_x + \boldsymbol{J}_B^{-1}\boldsymbol{\alpha}_2 + \boldsymbol{J}_B^{-1}\boldsymbol{z}_2 + \boldsymbol{d}\right] - \tilde{\boldsymbol{d}}^{+\mathrm{T}} \\ &\quad \left[\mathrm{Diag}\left(\mathrm{Tanh}\left(\frac{\boldsymbol{z}_1}{\boldsymbol{\varepsilon}_2}\right)\right)\boldsymbol{c}_e\boldsymbol{z}_1 - \hat{\boldsymbol{d}}^+\right] \\ &\quad + \tilde{k}\left[(k_u - k_l)\tanh\left(\frac{\boldsymbol{z}_1{}^{\mathrm{T}}\boldsymbol{z}_1}{\varepsilon_1}\right) - k_u + k\right]\end{aligned} \tag{52}$$

Then, the first virtual controller $\boldsymbol{\alpha}_2$ is designed as

$$\begin{aligned}\boldsymbol{\alpha}_2 = \boldsymbol{J}_B &\left[-c_1\boldsymbol{c}_e^{-1}\boldsymbol{z}_1 - \boldsymbol{F}_x - \hat{\boldsymbol{d}} - \mathrm{Diag}\left(\mathrm{Tanh}\left(\frac{\boldsymbol{z}_1}{\boldsymbol{\varepsilon}_2}\right)\right)\hat{\boldsymbol{d}}^+ - \tilde{k}(k_u - k_l)\frac{\boldsymbol{x}}{\varepsilon_1}\right]\end{aligned} \tag{53}$$

where $\boldsymbol{z}_2$ is the second auxiliary error and $c_1 > 0$. Thus, equation (52) can be rewritten as

$$\begin{aligned}\dot{V}_1 &= -c_1\|\boldsymbol{z}_1\|^2 + \boldsymbol{z}_1{}^{\mathrm{T}}\boldsymbol{c}_e\left[\boldsymbol{J}_B^{-1}\boldsymbol{z}_2 + \boldsymbol{d} - \hat{\boldsymbol{d}} - \mathrm{Diag}\left(\mathrm{Tanh}\left(\frac{\boldsymbol{z}_1}{\boldsymbol{\varepsilon}_2}\right)\right)\hat{\boldsymbol{d}}^+ - \tilde{k}(k_u - k_l)\frac{\boldsymbol{x}}{\varepsilon_1}\right] \\ &\quad - \tilde{\boldsymbol{d}}^{+\mathrm{T}}\left[\mathrm{Diag}\left(\mathrm{Tanh}\left(\frac{\boldsymbol{z}_1}{\boldsymbol{\varepsilon}_2}\right)\right)\boldsymbol{c}_e\boldsymbol{z}_1 - \hat{\boldsymbol{d}}^+\right] + \tilde{k}\left[(k_u - k_l)\tanh\left(\frac{\boldsymbol{z}_1{}^{\mathrm{T}}\boldsymbol{z}_1}{\varepsilon_1}\right) - k_u + k\right] \\ &= -c_1\|\boldsymbol{z}_1\|^2 + \boldsymbol{z}_1{}^{\mathrm{T}}\boldsymbol{c}_e\left[\boldsymbol{J}_B^{-1}\boldsymbol{z}_2 + \tilde{\boldsymbol{d}} - \mathrm{Diag}\left(\mathrm{Tanh}\left(\frac{\boldsymbol{z}_1}{\boldsymbol{\varepsilon}_2}\right)\right)\hat{\boldsymbol{d}}^+ - \mathrm{Diag}\left(\mathrm{Tanh}\left(\frac{\boldsymbol{z}_1}{\boldsymbol{\varepsilon}_2}\right)\right)\tilde{\boldsymbol{d}}^+\right] + \tilde{\boldsymbol{d}}^{+\mathrm{T}}\hat{\boldsymbol{d}}^+ \\ &\quad - \tilde{k}(k_u - k_l)\frac{\boldsymbol{z}_1{}^{\mathrm{T}}\boldsymbol{z}_1}{\varepsilon_1} + \tilde{k}\left[(k_u - k_l)\tanh\left(\frac{\boldsymbol{z}_1{}^{\mathrm{T}}\boldsymbol{z}_1}{\varepsilon_1}\right) + \tilde{k}\right] \\ &= -c_1\|\boldsymbol{z}_1\|^2 + \boldsymbol{z}_1{}^{\mathrm{T}}\boldsymbol{c}_e\left[\boldsymbol{J}_B^{-1}\boldsymbol{z}_2 + \tilde{\boldsymbol{d}} - \mathrm{Diag}\left(\mathrm{Tanh}\left(\frac{\boldsymbol{z}_1}{\boldsymbol{\varepsilon}_2}\right)\right)\boldsymbol{d}^+\right] + \tilde{\boldsymbol{d}}^{+\mathrm{T}}\hat{\boldsymbol{d}}^+ \\ &\quad - \tilde{k}(k_u - k_l)\left[\frac{\boldsymbol{z}_1{}^{\mathrm{T}}\boldsymbol{z}_1}{\varepsilon_1} - \tanh\left(\frac{\boldsymbol{z}_1{}^{\mathrm{T}}\boldsymbol{z}_1}{\varepsilon_1}\right)\right] + \|\tilde{k}\|^2\end{aligned} \tag{54}$$

The hyperbolic tangent function has the following property for any $\varepsilon > 0$ and any $m \in \boldsymbol{R}$ (Polycarpou and Ionannou, 1993)

$$0 \leqslant |m| - m\tanh\left(\frac{m}{\varepsilon}\right) \leqslant k_c\varepsilon \quad (k_c = 0.2785) \tag{55}$$

Using this property, the following is obtained

$$\begin{aligned} & \boldsymbol{z}_1{}^{\mathrm{T}}\boldsymbol{c}_e\left(\tilde{\boldsymbol{d}}-\mathrm{Diag}\left(\mathrm{Tanh}\left(\frac{\boldsymbol{z}_1}{\boldsymbol{\varepsilon}_2}\right)\right)\boldsymbol{d}^+\right) \\ &= \sum_{i=1}^{3}\left[\tilde{d}_i c_{ie} z_{1i} - d_i^+ z_{1i} c_{ie}\tanh\left(\frac{z_{1i}}{\varepsilon_{2i}}\right)\right] \\ &\leqslant \sum_{i=1}^{3} d_i^+ c_{ie}\left[|z_{1i}| - z_{1i}\tanh\left(\frac{z_{1i}}{\varepsilon_{2i}}\right)\right] \\ &\leqslant \sum_{i=1}^{3} d_i^+ c_{ie} k_c \varepsilon_{2i} = k_c \boldsymbol{d}^{+\mathrm{T}}\boldsymbol{c}_e\boldsymbol{\varepsilon}_2 \end{aligned} \tag{56}$$

Moreover, note the following facts

$$\begin{cases} \tilde{k}(k_u - k_l)\left[\frac{\boldsymbol{z}_1{}^{\mathrm{T}}\boldsymbol{z}_1}{\varepsilon_1} - \tanh\left(\frac{\boldsymbol{z}_1{}^{\mathrm{T}}\boldsymbol{z}_1}{\varepsilon_1}\right)\right] \geqslant 0 \\ \tilde{\boldsymbol{d}}^{+\mathrm{T}}\hat{\boldsymbol{d}}^+ = \tilde{\boldsymbol{d}}^{+\mathrm{T}}\boldsymbol{d}^+ - \tilde{\boldsymbol{d}}^{+\mathrm{T}}\tilde{\boldsymbol{d}}^+ \leqslant -\frac{1}{2}\left(\left\|\tilde{\boldsymbol{d}}^+\right\|^2 - \left\|\boldsymbol{d}^+\right\|^2\right) \end{cases} \tag{57}$$

Equation (54) can be rewritten as

$$\begin{aligned} \dot{V}_1 \leqslant & -c_1\|\boldsymbol{z}_1\|^2 + \boldsymbol{z}_1{}^{\mathrm{T}}\boldsymbol{c}_e\left(\boldsymbol{J}_B^{-1}\boldsymbol{z}_2\right) \\ & + k_c\boldsymbol{d}^{+\mathrm{T}}\boldsymbol{c}_e\boldsymbol{\varepsilon}_2 - \frac{1}{2}\left(\left\|\tilde{\boldsymbol{d}}^+\right\|^2 - \left\|\boldsymbol{d}^+\right\|^2\right) + \left\|\tilde{k}\right\|^2 \\ = & -c_1\|\boldsymbol{z}_1\|^2 - \gamma_2\frac{1}{2\gamma_2}\left\|\tilde{\boldsymbol{d}}^+\right\|^2 + \boldsymbol{z}_1{}^{\mathrm{T}}\boldsymbol{c}_e\left(\boldsymbol{J}_B^{-1}\boldsymbol{z}_2\right) \\ & + k_c\boldsymbol{d}^{+\mathrm{T}}\boldsymbol{c}_e\boldsymbol{\varepsilon}_2 + \frac{1}{2}\left\|\boldsymbol{d}^+\right\|^2 + \left\|\tilde{k}\right\|^2 \end{aligned} \tag{58}$$

To avoid the "explosion of terms" problem inherent in traditional backstepping control, a first-order filter is introduced to produce the derivative of the virtue controllers $\boldsymbol{\alpha}_2$. The output of the filter is defined as $\bar{\boldsymbol{\alpha}}_2$, and the dynamics of the filter is given by

$$\begin{cases} \tau_2\dot{\bar{\boldsymbol{\alpha}}}_2 + \bar{\boldsymbol{\alpha}}_2 = \boldsymbol{\alpha}_2 \\ \bar{\boldsymbol{\alpha}}_2(0) = \boldsymbol{\alpha}_2(0) \end{cases} \tag{59}$$

where τ_2 is a positive time constant. The error of the filter is defined as $\boldsymbol{e}_2 = \bar{\boldsymbol{\alpha}}_2 - \boldsymbol{\alpha}_2$. After taking time derivatives of $\boldsymbol{e}_2$ and $\boldsymbol{z}_2$, the following is obtained

$$\begin{cases} \dot{\boldsymbol{e}}_2 = \dot{\bar{\boldsymbol{\alpha}}}_2 - \dot{\boldsymbol{\alpha}}_2 = \dfrac{\boldsymbol{\alpha}_2 - \bar{\boldsymbol{\alpha}}_2}{\tau_2} - \dot{\boldsymbol{\alpha}}_2 = -\dfrac{\boldsymbol{e}_2}{\tau_2} + \boldsymbol{b}_2 \\ \dot{\boldsymbol{z}}_2 = \dfrac{\partial g}{\partial \boldsymbol{v}}\dot{\boldsymbol{v}} - \dot{\boldsymbol{\alpha}}_2 = f(\boldsymbol{w}) - \dot{\boldsymbol{\alpha}}_2 = f(\boldsymbol{w}) - \dot{\bar{\boldsymbol{\alpha}}}_2 + \dot{\boldsymbol{e}}_2 \end{cases} \tag{60}$$

where $\boldsymbol{b}_2 = -\dot{\boldsymbol{\alpha}}_2$.

Step 2: Design of the virtual controller for $f(\boldsymbol{w})$. The second virtual controller $\boldsymbol{\alpha}_3$ is defined as $\boldsymbol{\alpha}_3 = f(\boldsymbol{w}) - \boldsymbol{z}_3$. The second Lyapunov function for $\boldsymbol{z}_2$ is designed as

$$V_2 = V_1 + \frac{1}{2}\boldsymbol{z}_2{}^{\mathrm{T}}\boldsymbol{z}_2 + \frac{1}{2}\boldsymbol{e}_2{}^{\mathrm{T}}\boldsymbol{e}_2 \tag{61}$$

After taking the time derivative of (61) and combining it with (60), the following is obtained

$$\begin{aligned} \dot{V}_2 = & \dot{V}_1 + \boldsymbol{z}_2{}^{\mathrm{T}}\dot{\boldsymbol{z}}_2 + \boldsymbol{e}_2{}^{\mathrm{T}}\dot{\boldsymbol{e}}_2 = \dot{V}_1 \\ & + \boldsymbol{z}_2{}^{\mathrm{T}}\left(f(\boldsymbol{w}) - \dot{\bar{\boldsymbol{\alpha}}}_2 + \dot{\boldsymbol{e}}_2\right) + \boldsymbol{e}_2{}^{\mathrm{T}}\left(-\frac{\boldsymbol{e}_2}{\tau_2} + \boldsymbol{b}_2\right) \\ \leqslant & -c_1\|\boldsymbol{z}_1\|^2 - \gamma_2\frac{1}{2\gamma_2}\left\|\tilde{\boldsymbol{d}}^+\right\|^2 \\ & + \boldsymbol{z}_1{}^{\mathrm{T}}\boldsymbol{c}_e\left(\boldsymbol{J}_B^{-1}\boldsymbol{z}_2\right) + k_c\boldsymbol{d}^{+\mathrm{T}}\boldsymbol{c}_e\boldsymbol{\varepsilon}_2 + \frac{1}{2}\left\|\boldsymbol{d}^+\right\|^2 + \left\|\tilde{k}\right\|^2 \\ & + \boldsymbol{z}_2{}^{\mathrm{T}}\left(\boldsymbol{\alpha}_3 + \boldsymbol{z}_3 - \dot{\bar{\boldsymbol{\alpha}}}_2 + \dot{\boldsymbol{e}}_2\right) + \boldsymbol{e}_2{}^{\mathrm{T}}\left(-\frac{\boldsymbol{e}_2}{\tau_2} + \boldsymbol{b}_2\right) \end{aligned} \tag{62}$$

Then, the second virtual controller $\boldsymbol{\alpha}_3$ is designed as

$$\boldsymbol{\alpha}_3 = -c_2\boldsymbol{z}_2 - \boldsymbol{J}_B^{-1}\boldsymbol{c}_e\boldsymbol{z}_1 + \dot{\bar{\boldsymbol{\alpha}}}_2 \tag{63}$$

where $\boldsymbol{z}_3$ is the third auxiliary error and $c_2 > 0$. Thus, equation (62) can be rewritten as

$$\begin{aligned} \dot{V}_2 \leqslant & -c_1\|\boldsymbol{z}_1\|^2 - \gamma_2\frac{1}{2\gamma_2}\left\|\tilde{\boldsymbol{d}}^+\right\|^2 + \boldsymbol{z}_1{}^{\mathrm{T}}\boldsymbol{c}_e\left(\boldsymbol{J}_B^{-1}\boldsymbol{z}_2\right) \\ & + k_c\boldsymbol{d}^{+\mathrm{T}}\boldsymbol{c}_e\boldsymbol{\varepsilon}_2 + \frac{1}{2}\left\|\boldsymbol{d}^+\right\|^2 + \left\|\tilde{k}\right\|^2 \\ & + \boldsymbol{z}_2{}^{\mathrm{T}}\left(-c_2\boldsymbol{z}_2 - \boldsymbol{J}_B^{-1}\boldsymbol{c}_e\boldsymbol{z}_1 + \dot{\bar{\boldsymbol{\alpha}}}_2 + \boldsymbol{z}_3 - \dot{\bar{\boldsymbol{\alpha}}}_2 + \dot{\boldsymbol{e}}_2\right) \\ & + \boldsymbol{e}_2{}^{\mathrm{T}}\left(-\frac{\boldsymbol{e}_2}{\tau_2} + \boldsymbol{b}_2\right) \\ = & -\sum_{i=1}^{2} c_i\|\boldsymbol{z}_i\|^2 - \gamma_2\frac{1}{2\gamma_2}\left\|\tilde{\boldsymbol{d}}^+\right\|^2 + k_c\boldsymbol{d}^{+\mathrm{T}}\boldsymbol{c}_e\boldsymbol{\varepsilon}_2 \\ & + \frac{1}{2}\left\|\boldsymbol{d}^+\right\|^2 + \left\|\tilde{k}\right\|^2 + \boldsymbol{z}_2{}^{\mathrm{T}}(\boldsymbol{z}_3 + \dot{\boldsymbol{e}}_2) + \boldsymbol{e}_2{}^{\mathrm{T}}\left(-\frac{\boldsymbol{e}_2}{\tau_2} + \boldsymbol{b}_2\right) \end{aligned} \tag{64}$$

The second first-order filter is introduced to produce the derivative of the virtue controllers $\boldsymbol{\alpha}_3$. The output of the filter is defined as $\bar{\boldsymbol{\alpha}}_3$. The dynamics of the filter is given by

$$\begin{cases} \tau_3\dot{\bar{\boldsymbol{\alpha}}}_3 + \bar{\boldsymbol{\alpha}}_3 = \boldsymbol{\alpha}_3 \\ \bar{\boldsymbol{\alpha}}_3(0) = \boldsymbol{\alpha}_3(0) \end{cases} \tag{65}$$

where τ_3 is a positive time constant. The error of the filter is defined as $\boldsymbol{e}_3 = \bar{\boldsymbol{\alpha}}_3 - \boldsymbol{\alpha}_3$. After taking time derivatives of $\boldsymbol{e}_3$ and $\boldsymbol{z}_3$, the following is obtained

$$\begin{cases} \dot{\boldsymbol{e}}_3 = \dot{\bar{\boldsymbol{\alpha}}}_3 - \dot{\boldsymbol{\alpha}}_3 = \dfrac{\boldsymbol{\alpha}_3 - \bar{\boldsymbol{\alpha}}_3}{\tau_3} - \dot{\boldsymbol{\alpha}}_3 = -\dfrac{\boldsymbol{e}_3}{\tau_3} + \boldsymbol{b}_3 \\ \dot{\boldsymbol{z}}_3 = \dfrac{\partial f}{\partial \boldsymbol{w}}\dot{\boldsymbol{w}} - \dot{\boldsymbol{\alpha}}_3 = h(\boldsymbol{q}) - \dot{\boldsymbol{\alpha}}_3 = h(\boldsymbol{q}) - \dot{\bar{\boldsymbol{\alpha}}}_3 + \dot{\boldsymbol{e}}_3 \end{cases} \tag{66}$$

where $\boldsymbol{b}_3 = -\dot{\boldsymbol{\alpha}}_3$.

Step 3: Design of the virtual controller for $h(\boldsymbol{q})$. The third virtual controller $\boldsymbol{\alpha}_4$ is defined as $\boldsymbol{\alpha}_4 = h(\boldsymbol{q}) - \boldsymbol{z}_4$. The third Lyapunov function for $\boldsymbol{z}_3$ is designed as

$$V_3 = V_2 + \frac{1}{2}\boldsymbol{z}_3{}^{\mathrm{T}}\boldsymbol{z}_3 + \frac{1}{2}\boldsymbol{e}_3{}^{\mathrm{T}}\boldsymbol{e}_3 \tag{67}$$

After taking the time derivative of (67) and combining it with (66), the following is obtained

$$\begin{aligned}\dot{V}_3 &= \dot{V}_2 + \boldsymbol{z}_3^{\mathrm{T}}\dot{\boldsymbol{z}}_3 + \boldsymbol{e}_3^{\mathrm{T}}\dot{\boldsymbol{e}}_3 = \dot{V}_2 + \boldsymbol{z}_3^{\mathrm{T}}\left(h(\boldsymbol{q}) - \dot{\bar{\boldsymbol{\alpha}}}_3 + \dot{\boldsymbol{e}}_3\right) \\ &\quad + \boldsymbol{e}_3^{\mathrm{T}}\left(-\frac{\boldsymbol{e}_3}{\tau_3} + \boldsymbol{b}_3\right) \\ &\leqslant -\sum_{i=1}^{2} c_i\|\boldsymbol{z}_i\|^2 - \gamma_2\frac{1}{2\gamma_2}\left\|\tilde{\boldsymbol{d}}^+\right\|^2 + k_c\boldsymbol{d}^{+\mathrm{T}}\boldsymbol{c}_e\boldsymbol{\varepsilon}_2 \\ &\quad + \frac{1}{2}\left\|\boldsymbol{d}^+\right\|^2 + \left\|\tilde{k}\right\|^2 + \boldsymbol{z}_2^{\mathrm{T}}(\boldsymbol{z}_3 + \dot{\boldsymbol{e}}_2) \\ &\quad + \sum_{i=2}^{3}\boldsymbol{e}_i^{\mathrm{T}}\left(-\frac{\boldsymbol{e}_i}{\tau_i} + \boldsymbol{b}_i\right) + \boldsymbol{z}_3^{\mathrm{T}}\left(\boldsymbol{\alpha}_4 + \boldsymbol{z}_4 - \dot{\bar{\boldsymbol{\alpha}}}_3 + \dot{\boldsymbol{e}}_3\right)\end{aligned} \tag{68}$$

Then, the third virtual controller $\boldsymbol{\alpha}_4$ is designed as

$$\boldsymbol{\alpha}_4 = -c_3\boldsymbol{z}_3 - \boldsymbol{z}_2 + \dot{\bar{\boldsymbol{\alpha}}}_3 \tag{69}$$

where $\boldsymbol{z}_4$ is the third auxiliary error and $c_3 > 0$. Thus, equation (68) can be rewritten as

$$\begin{aligned}\dot{V}_2 &\leqslant -\sum_{i=1}^{2} c_i\|\boldsymbol{z}_i\|^2 - \gamma_2\frac{1}{2\gamma_2}\left\|\tilde{\boldsymbol{d}}^+\right\|^2 + k_c\boldsymbol{d}^{+\mathrm{T}}\boldsymbol{c}_e\boldsymbol{\varepsilon}_2 \\ &\quad + \frac{1}{2}\left\|\boldsymbol{d}^+\right\|^2 + \left\|\tilde{k}\right\|^2 + \boldsymbol{z}_2^{\mathrm{T}}(\boldsymbol{z}_3 + \dot{\boldsymbol{e}}_2) \\ &\quad + \sum_{i=2}^{3}\boldsymbol{e}_i^{\mathrm{T}}\left(-\frac{\boldsymbol{e}_i}{\tau_i} + \boldsymbol{b}_i\right) \\ &\quad + \boldsymbol{z}_3^{\mathrm{T}}\left(-c_3\boldsymbol{z}_3 - \boldsymbol{z}_2 + \dot{\bar{\boldsymbol{\alpha}}}_3 + \boldsymbol{z}_4 - \dot{\bar{\boldsymbol{\alpha}}}_3 + \dot{\boldsymbol{e}}_3\right) \\ &= -\sum_{i=1}^{3} c_i\|\boldsymbol{z}_i\|^2 - \gamma_2\frac{1}{2\gamma_2}\left\|\tilde{\boldsymbol{d}}^+\right\|^2 \\ &\quad + k_c\boldsymbol{d}^{+\mathrm{T}}\boldsymbol{c}_e\boldsymbol{\varepsilon}_2 + \frac{1}{2}\left\|\boldsymbol{d}^+\right\|^2 + \left\|\tilde{k}\right\|^2 + \boldsymbol{z}_2^{\mathrm{T}}\dot{\boldsymbol{e}}_2 + \boldsymbol{z}_3^{\mathrm{T}}(\boldsymbol{z}_4 + \dot{\boldsymbol{e}}_3) \\ &\quad + \sum_{i=2}^{3}\boldsymbol{e}_i^{\mathrm{T}}\left(-\frac{\boldsymbol{e}_i}{\tau_i} + \boldsymbol{b}_i\right)\end{aligned} \tag{70}$$

The third first-order filter is introduced to produce the derivative of the virtue controllers $\boldsymbol{\alpha}_4$. The output of the filter is defined as $\bar{\boldsymbol{\alpha}}_4$. The dynamics of the filter is given by

$$\begin{cases}\tau_4\dot{\bar{\boldsymbol{\alpha}}}_4 + \bar{\boldsymbol{\alpha}}_4 = \boldsymbol{\alpha}_4 \\ \bar{\boldsymbol{\alpha}}_4(0) = \boldsymbol{\alpha}_4(0)\end{cases} \tag{71}$$

where τ_4 is a positive time constant. The error of the filter is defined as $\boldsymbol{e}_4 = \bar{\boldsymbol{\alpha}}_4 - \boldsymbol{\alpha}_4$. After taking time derivatives of $\boldsymbol{e}_4$ and $\boldsymbol{z}_4$, the following is obtained

$$\begin{cases}\dot{\boldsymbol{e}}_4 = \dot{\bar{\boldsymbol{\alpha}}}_4 - \dot{\boldsymbol{\alpha}}_4 = \dfrac{\boldsymbol{\alpha}_4 - \bar{\boldsymbol{\alpha}}_4}{\tau_4} - \dot{\boldsymbol{\alpha}}_4 = -\dfrac{\boldsymbol{e}_4}{\tau_4} + \boldsymbol{b}_4 \\ \dot{\boldsymbol{z}}_4 = \dfrac{\partial h}{\partial \boldsymbol{q}}\dot{\boldsymbol{q}} - \dot{\boldsymbol{\alpha}}_4 = \boldsymbol{\mu} - \dot{\boldsymbol{\alpha}}_4 = \boldsymbol{\mu} - \dot{\bar{\boldsymbol{\alpha}}}_4 + \dot{\boldsymbol{e}}_4\end{cases} \tag{72}$$

where $\boldsymbol{b}_4 = -\dot{\boldsymbol{\alpha}}_4$.

Step 4: Design of the control law for $\boldsymbol{\mu}$. The fourth Lyapunov function for $\boldsymbol{z}_4$ is designed as

$$V_4 = V_3 + \frac{1}{2}\boldsymbol{z}_4^{\mathrm{T}}\boldsymbol{z}_4 + \frac{1}{2}\boldsymbol{e}_4^{\mathrm{T}}\boldsymbol{e}_4 \tag{73}$$

After taking the time derivative of (73) and combining (71) and (72), the following is obtained

$$\begin{aligned}\dot{V}_4 &= \dot{V}_3 + \boldsymbol{z}_4^{\mathrm{T}}\dot{\boldsymbol{z}}_4 + \boldsymbol{e}_4^{\mathrm{T}}\dot{\boldsymbol{e}}_4 = \dot{V}_3 \\ &\quad + \boldsymbol{z}_4^{\mathrm{T}}\left(\boldsymbol{\mu} - \dot{\bar{\boldsymbol{\alpha}}}_4 + \dot{\boldsymbol{e}}_4\right) + \boldsymbol{e}_4^{\mathrm{T}}\left(-\frac{\boldsymbol{e}_4}{\tau_4} + \boldsymbol{b}_4\right) \\ &\leqslant -\sum_{i=1}^{3} c_i\|\boldsymbol{z}_i\|^2 - \gamma_2\frac{1}{2\gamma_2}\left\|\tilde{\boldsymbol{d}}^+\right\|^2 + k_c\boldsymbol{d}^{+\mathrm{T}}\boldsymbol{c}_e\boldsymbol{\varepsilon}_2 \\ &\quad + \frac{1}{2}\left\|\boldsymbol{d}^+\right\|^2 + \left\|\tilde{k}\right\|^2 + \boldsymbol{z}_2^{\mathrm{T}}\dot{\boldsymbol{e}}_2 \\ &\quad + \boldsymbol{z}_3^{\mathrm{T}}(\boldsymbol{z}_4 + \dot{\boldsymbol{e}}_3) + \boldsymbol{z}_4^{\mathrm{T}}\left(\boldsymbol{\mu} - \dot{\bar{\boldsymbol{\alpha}}}_4 + \dot{\boldsymbol{e}}_4\right) \\ &\quad + \sum_{i=2}^{4}\boldsymbol{e}_i^{\mathrm{T}}\left(-\frac{\boldsymbol{e}_i}{\tau_i} + \boldsymbol{b}_i\right)\end{aligned} \tag{74}$$

Then, the control law $\boldsymbol{\mu}$ is designed as

$$\boldsymbol{\mu} = -c_4\boldsymbol{z}_4 - \boldsymbol{z}_3 + \dot{\bar{\boldsymbol{\alpha}}}_4 \tag{75}$$

where $c_4 > 0$. Thus, equation (74) can be rewritten as

$$\begin{aligned}\dot{V}_4 &\leqslant -\sum_{i=1}^{3} c_i\|\boldsymbol{z}_i\|^2 - \gamma_2\frac{1}{2\gamma_2}\left\|\tilde{\boldsymbol{d}}^+\right\|^2 + k_c\boldsymbol{d}^{+\mathrm{T}}\boldsymbol{c}_e\boldsymbol{\varepsilon}_2 \\ &\quad + \frac{1}{2}\left\|\boldsymbol{d}^+\right\|^2 + \left\|\tilde{k}\right\|^2 + \boldsymbol{z}_2^{\mathrm{T}}\dot{\boldsymbol{e}}_2 \\ &\quad + \boldsymbol{z}_3^{\mathrm{T}}(\boldsymbol{z}_4 + \dot{\boldsymbol{e}}_3) + \boldsymbol{z}_4^{\mathrm{T}}\left(-c_4\boldsymbol{z}_4 - \boldsymbol{z}_3 + \dot{\bar{\boldsymbol{\alpha}}}_4 - \dot{\bar{\boldsymbol{\alpha}}}_4 + \dot{\boldsymbol{e}}_4\right) \\ &\quad + \sum_{i=2}^{4}\boldsymbol{e}_i^{\mathrm{T}}\left(-\frac{\boldsymbol{e}_i}{\tau_i} + \boldsymbol{b}_i\right) \\ &= -\sum_{i=1}^{4} c_i\|\boldsymbol{z}_i\|^2 - \gamma_2\frac{1}{2\gamma_2}\left\|\tilde{\boldsymbol{d}}^+\right\|^2 + k_c\boldsymbol{d}^{+\mathrm{T}}\boldsymbol{c}_e\boldsymbol{\varepsilon}_2 \\ &\quad + \frac{1}{2}\left\|\boldsymbol{d}^+\right\|^2 + \left\|\tilde{k}\right\|^2 + \sum_{i=2}^{4}\boldsymbol{z}_i^{\mathrm{T}}\dot{\boldsymbol{e}}_i + \sum_{i=2}^{4}\boldsymbol{e}_i^{\mathrm{T}}\left(-\frac{\boldsymbol{e}_i}{\tau_i} + \boldsymbol{b}_i\right) \\ &= -\sum_{i=1}^{4} c_i\|\boldsymbol{z}_i\|^2 + \sum_{i=2}^{4}\boldsymbol{z}_i^{\mathrm{T}}\left(-\frac{\boldsymbol{e}_i}{\tau_i} + \boldsymbol{b}_i\right) \\ &\quad + \sum_{i=2}^{4}\boldsymbol{e}_i^{\mathrm{T}}\left(-\frac{\boldsymbol{e}_i}{\tau_i} + \boldsymbol{b}_i\right) - \gamma_2\frac{1}{2\gamma_2}\left\|\tilde{\boldsymbol{d}}^+\right\|^2 + k_c\boldsymbol{d}^{+\mathrm{T}}\boldsymbol{c}_e\boldsymbol{\varepsilon}_2 \\ &\quad + \frac{1}{2}\left\|\boldsymbol{d}^+\right\|^2 + \left\|\tilde{k}\right\|^2\end{aligned} \tag{76}$$

Note the following facts

$$\begin{cases}\displaystyle\sum_{i=2}^{4}\boldsymbol{z}_i^{\mathrm{T}}\left(-\frac{\boldsymbol{e}_i}{\tau_i} + \boldsymbol{b}_i\right) \leqslant \sum_{i=2}^{4}\frac{1}{2\tau_i}\left(\|\boldsymbol{z}_i\|^2 + \|\boldsymbol{e}_i\|^2\right) + \sum_{i=2}^{4}\frac{1}{2\rho}\|\boldsymbol{z}_i\|^2\|\boldsymbol{b}_i\|^2 + \frac{3}{2}\rho \\ \displaystyle\sum_{i=2}^{4}\boldsymbol{e}_i^{\mathrm{T}}\left(-\frac{\boldsymbol{e}_i}{\tau_i} + \boldsymbol{b}_i\right) \leqslant -\sum_{i=2}^{4}\frac{1}{\tau_i}\|\boldsymbol{e}_i\|^2 + \sum_{i=2}^{4}\frac{1}{2\rho}\|\boldsymbol{e}_i\|^2\|\boldsymbol{b}_i\|^2 + \frac{3}{2}\rho\end{cases} \tag{77}$$

where $\rho > 0$. Thus, equation (76) can be rewritten as

$$\begin{aligned}\dot{V}_4 \leqslant & -\sum_{i=1}^{4} c_i\|\boldsymbol{z}_i\|^2 + \sum_{i=2}^{4}\frac{1}{2\tau_i}\left(\|\boldsymbol{z}_i\|^2 + \|\boldsymbol{e}_i\|^2\right) \\ & + \sum_{i=2}^{4}\frac{1}{2\rho}\|\boldsymbol{z}_i\|^2\|\boldsymbol{b}_i\|^2 + \frac{3}{2}\rho \\ & - \sum_{i=2}^{4}\frac{1}{\tau_i}\|\boldsymbol{e}_i\|^2 + \sum_{i=2}^{4}\frac{1}{2\rho}\|\boldsymbol{e}_i\|^2\|\boldsymbol{b}_i\|^2 + \frac{3}{2}\rho \\ & - \gamma_2\frac{1}{2\gamma_2}\left\|\tilde{\boldsymbol{d}}^+\right\|^2 + k_c\boldsymbol{d}^{+\mathrm{T}}\boldsymbol{c}_e\boldsymbol{\varepsilon}_2 + \frac{1}{2}\left\|\boldsymbol{d}^+\right\|^2 + \left\|\tilde{k}\right\|^2 \\ = & -c_1\|\boldsymbol{z}_1\|^2 - \sum_{i=2}^{4}\left(c_i - \frac{1}{2\tau_i} - \frac{1}{2\rho}\|\boldsymbol{b}_i\|^2\right)\|\boldsymbol{z}_i\|^2 \\ & - \sum_{i=2}^{4}\left(\frac{1}{2\tau_i} - \frac{1}{2\rho}\|\boldsymbol{b}_i\|^2\right)\|\boldsymbol{e}_i\|^2 \\ & - \gamma_2\frac{1}{2\gamma_2}\left\|\tilde{\boldsymbol{d}}^+\right\|^2 - 2\gamma_1\frac{1}{2\gamma_1}k^2 + \frac{1}{2}\left\|\boldsymbol{d}^+\right\|^2 \\ & + k_u\boldsymbol{d}^{+\mathrm{T}}\boldsymbol{C}\boldsymbol{\varepsilon}_2 + 3\rho\end{aligned} \tag{78}$$

Assumption 6: The desired attitude signal, its first derivative, and its second derivative are assumed to be smooth bounded functions during the whole attitude control process.

Two compact sets are defined:

$$\begin{aligned}\boldsymbol{\Omega}_1 &= \{\boldsymbol{x}_d = k\boldsymbol{\sigma}_d + \boldsymbol{\omega}_d | \boldsymbol{x}_d + \dot{\boldsymbol{x}}_d + \ddot{\boldsymbol{x}}_d \leqslant \boldsymbol{R}_0\} \\ \boldsymbol{\Omega}_2 &= \left\{\tfrac{1}{2}\sum_{i=1}^{4}\boldsymbol{z}_i^{\mathrm{T}}\boldsymbol{z}_i + \tfrac{1}{2}\sum_{i=2}^{4}\boldsymbol{e}_i^{\mathrm{T}}\boldsymbol{e}_i + \tfrac{1}{2\gamma_2}\tilde{\boldsymbol{d}}^{+\mathrm{T}}\tilde{\boldsymbol{d}}^+ + \tfrac{1}{2\gamma_1}k^2 \leqslant 2\vartheta\right\}\end{aligned} \tag{79}$$

where $\vartheta > 0$. Thus, the smooth vectors $\boldsymbol{b}_2$, $\boldsymbol{b}_3$, and $\boldsymbol{b}_4$ are bounded on $\boldsymbol{\Omega}_1 \times \boldsymbol{\Omega}_2$, that is, there exist positive constants B_2, B_3, and B_4 such that $\|\boldsymbol{b}_2\| \leqslant B_2$, $\|\boldsymbol{b}_3\| \leqslant B_3$, and $\|\boldsymbol{b}_4\| \leqslant B_4$ (Butt et al., 2013, 2015).

Thereafter, a constant $\varphi > 0$ is defined and

$$\begin{aligned}&c_1 \geqslant \varphi\ ,\ \gamma_1 \geqslant \varphi\ \ \gamma_2 \geqslant 2\varphi\ ,\ c_i \geqslant \frac{1}{2\tau_i} + \frac{1}{2\rho}B_i^2 + \varphi\ , \\ &\frac{1}{\tau_i} \geqslant \frac{1}{\rho}B_i^2 + 2\varphi\ \ (i = 2,3,4)\end{aligned} \tag{80}$$

is chosen.

Thus, equation (78) follows

$$\begin{aligned}\dot{V}_4 \leqslant & -\varphi\sum_{i=1}^{4}\|\boldsymbol{z}_i\|^2 - \varphi\sum_{i=2}^{4}\|\boldsymbol{e}_i\|^2 - \varphi\frac{1}{\gamma_1}k^2 \\ & - \varphi\frac{1}{\gamma_2}\left\|\tilde{\boldsymbol{d}}^+\right\|^2 + \frac{1}{2}\left\|\boldsymbol{d}^+\right\|^2 + k_c\boldsymbol{d}^{+\mathrm{T}}\boldsymbol{c}_e\boldsymbol{\varepsilon}_2 + 3\rho \\ = & -2\varphi V + \phi\end{aligned} \tag{81}$$

where $\phi = 0.5\left\|\boldsymbol{d}^+\right\|^2 + k_c\boldsymbol{d}^{+\mathrm{T}}\boldsymbol{c}_e\boldsymbol{\varepsilon}_2 + 3\rho$. If the proper φ satisfying $\varphi > \phi/(2\vartheta)$ is chosen, then $\dot{V}_4 \leqslant 0$ in $V_4 = \vartheta$; in this sense, $V_4 \leqslant \vartheta$ is an invariant set, which thus guarantees that for any $V_4(0) \leqslant \vartheta$, $V_4(t) \leqslant \vartheta$ for all $t \geqslant 0$. Actually, because it is always impossible for practical states to be infinite in engineering, this initial condition is indeed not restrictive as long as ϑ is chosen to be sufficiently large (Gao et al., 2016).

From (73) and (81), the following is obtained

$$0 \leqslant V(t) \leqslant \frac{\phi}{2\varphi} + \left(V(0) - \frac{\phi}{2\varphi}\right)e^{-2\varphi t} \tag{82}$$

which implies that there exists a time moment T such that for any $t > T$, $0 \leqslant V \leqslant \phi/(2\varphi)$. In view of the definition of V, the attitude error ultimately converges to the compact set

$$\boldsymbol{\Omega}_3 = \left\{\boldsymbol{\Psi} = (\boldsymbol{\sigma}_e,\ \boldsymbol{\omega}_e)^{\mathrm{T}} | \|\boldsymbol{\Psi}\| \leqslant \sqrt{\frac{\phi}{\varphi}}\right\} \tag{83}$$

Thus, it can be concluded that the attitude error can be adjusted to be arbitrarily small by choosing the proper parameters $\boldsymbol{\varepsilon}_2$, $\boldsymbol{c}_e$, and ρ.

It is to be noted that the dynamics of the auxiliary control signals $\boldsymbol{v}$ and $\boldsymbol{w}$ are derived based on the facts that $\dot{\boldsymbol{u}}_t = f(\boldsymbol{w}) = \frac{\partial g}{\partial \boldsymbol{v}}\dot{\boldsymbol{v}}$ and $\ddot{\boldsymbol{u}}_t = h(\boldsymbol{q}) = \frac{\partial f}{\partial \boldsymbol{w}}\dot{\boldsymbol{w}}$. This means that $\int h(\boldsymbol{q})\,\mathrm{d}t = f(\boldsymbol{w})$ and $\int f(\boldsymbol{w})\,\mathrm{d}t = g(\boldsymbol{v})$, and the derivation relations of $g(\boldsymbol{v})$, $f(\boldsymbol{w})$, and $h(\boldsymbol{q})$ can be satisfied.

Remark 2: The convergence region is determined by the upper bounds of the observer error and the parameters $\boldsymbol{\varepsilon}_2$, $\boldsymbol{c}_e$, and ρ (Swaroop et al., 2000; Wang and Jie, 2005). The principle of tradeoff must be used to choose the parameters to avoid the possible occurrence of the overshoot of two actuators and the chattering problem in practical application.

Remark 3: To obtain the ideal control torque $\boldsymbol{u}_t$, the initial conditions of the auxiliary control signals $\boldsymbol{v}$, $\boldsymbol{w}$, and $\boldsymbol{q}$ should first be given by $\boldsymbol{v}_0$, $\boldsymbol{w}_0$, and $\boldsymbol{q}_0$. By combining the control law $\boldsymbol{\mu}$ in (75) and the dynamic of $\boldsymbol{q}$ in (43), the control signals $\boldsymbol{q}$ and $h(\boldsymbol{q})$ can be updated. Then, by combining $h(\boldsymbol{q})$ and the dynamic of $\boldsymbol{w}$ in (45), the control signals $\boldsymbol{w}$ and $f(\boldsymbol{w})$ can be updated. Next, by combining $f(\boldsymbol{w})$ and the dynamic of $\boldsymbol{v}$ in (44), the control signals $\boldsymbol{v}$ and $g(\boldsymbol{v})$ can be updated. Thus, the ideal control torque $\boldsymbol{u}_t$ is obtained by (40).

Analysis of hard constraints on actuators

As is known, constraints can be soft or hard. Hard constraints cannot be violated, whereas soft constraints can be violated. Although only soft constraints can be imposed on the movement of masses by the above control algorithm, fortunately, it is sufficient for the speed and acceleration of each mass. However, as there are physical limits on the two actuators, hard constraints must be imposed on the position of each mass and the magnetic moment generated by the magnetorquer.

Not considering hard constraints might lead to severe discrepancies between the commanded input signals and actual control signals. Thus, it is important to deal with the control errors when hard constraints are imposed on practical actuators.

Hard constraints on the position l_i and the magnetic moment m_{Bi} can be respectively expressed as

$$l_i^a = \begin{cases} l_i^u \tanh\left(\frac{l_i}{l_i^u}\right), & l_i \geqslant 0 \\ l_i^l \tanh\left(\frac{l_i}{l_i^l}\right), & l_i < 0 \end{cases}, \qquad m_{Bi}^a = \begin{cases} m_{Bi}^u, & m_{Bi} > m_{Bi}^u \\ m_{Bi}, & m_{Bi}^l \leqslant m_{Bi} \leqslant m_{Bi}^u, \\ m_{Bi}^l, & m_{Bi} < m_{Bi}^l \end{cases} \quad (i = 1, 2, 3) \tag{84}$$

where l_i^a denotes the actual position signal of each linear motor, $l_i^u > 0$ and $l_i^l < 0$ are the upper and lower bounds of the position, respectively, m_{Bi}^a denotes the actual magnetic moment signal of the magnetorquer, m_{Bi}^u and m_{Bi}^l are the upper and lower bounds of the magnetic moment, respectively. To prevent the sudden change of position, the smooth hyperbolic tangent function is used to replace the sign function to limit the actual position signals.

As the magnitude of the ideal control torque is strictly limited by the control law, the overshoot of the position or the magnetic moment only occurs occasionally, and even if it occurs, the value will be small. The torque difference between command input signals and actual control signals is seen as another source of disturbance that can be observed.

The actual control input $\boldsymbol{u}_t^a$ and the disturbance $\boldsymbol{d}_c$ caused by control error are defined as

$$\boldsymbol{u}_t^a = -\boldsymbol{r}_s^a \times \boldsymbol{F}_{aero} + \boldsymbol{m}_B^a \times \boldsymbol{B} \tag{85}$$

$$\boldsymbol{d}_c = -\left[\boldsymbol{u}_t - \left(-\boldsymbol{r}_s^a \times \boldsymbol{F}_{aero} + \boldsymbol{m}_B^a \times \boldsymbol{B}\right)\right] \tag{86}$$

where $\boldsymbol{r}_s^a$ is the actual command position of the CoM, and $\boldsymbol{m}_B^a$ is the actual command magnetic moment.

Hence, the total disturbance $\boldsymbol{d}$ is

$$\boldsymbol{d} = \boldsymbol{d}_s + \boldsymbol{J}^{-1}\boldsymbol{d}_c \tag{87}$$

where

$$\begin{aligned} \boldsymbol{d}_s = &-\boldsymbol{J}^{-1}[\boldsymbol{r}_s \times \Delta\boldsymbol{F}_{aero} + \Delta\boldsymbol{r}_s \times (\boldsymbol{F}_{aero} + \Delta\boldsymbol{F}_{aero})] \\ &+ \boldsymbol{J}^{-1}(\Delta\boldsymbol{m}_B \times \boldsymbol{B} + \Delta\boldsymbol{d} + \boldsymbol{M}_{xt}) \end{aligned} \tag{88}$$

Thus, the simplified system model becomes

$$\dot{\boldsymbol{x}} = \boldsymbol{F}_x + \boldsymbol{J}_B^{-1}\boldsymbol{u}_t^a + \boldsymbol{d} \tag{89}$$

Theorem 2: Consider system (89) with the nonlinear observer given in (31) and the proposed backstepping control laws in (75) with hard constraints on actuators shown in (84). By choosing the proper control parameters in (80), the attitude error will converge to zero, and the output of the actuators will be prevented from overshooting via the compensation of the observer.

Proof: The proof of Theorem 2 is similar to that of Theorem 1, and is therefore omitted here.

Control allocation

The vector $\boldsymbol{v}_a^b$ is defined as the relative flow vector expressed in the $O_BX_BY_BZ_B$ system, and $\hat{\boldsymbol{v}}_a^b$ is the unit vector of $\boldsymbol{v}_a^b$. With the assumption that the relative flow vector expressed in the $O_OX_OY_OZ_O$ system is $[-1, 0, 0]^T$, $\boldsymbol{v}_a^b$ and $\hat{\boldsymbol{v}}_a^b$ are given by

$$\boldsymbol{v}_a^b = \boldsymbol{A}_{bo}\begin{bmatrix} -1 \\ 0 \\ 0 \end{bmatrix}, \qquad \hat{\boldsymbol{v}}_a^b = \frac{\boldsymbol{v}_a^b}{\|\boldsymbol{v}_a^b\|} \tag{90}$$

As shown in Figure 3(a), planes $\boldsymbol{\beta}_1$ and $\boldsymbol{\beta}_2$ are perpendicular to the geomagnetic field vector $\boldsymbol{B}$ and the relative flow vector $\boldsymbol{v}_a^b$, respectively. Additionally, line ϕ_l is the intersection line of planes $\boldsymbol{\beta}_1$ and $\boldsymbol{\beta}_2$. The control torque $\boldsymbol{u}_t$ on the plane $\boldsymbol{\beta}_3$ can be decomposed as

$$\boldsymbol{u}_t = \boldsymbol{u}_{t\perp B} + \boldsymbol{u}_{t\parallel B} \tag{91}$$

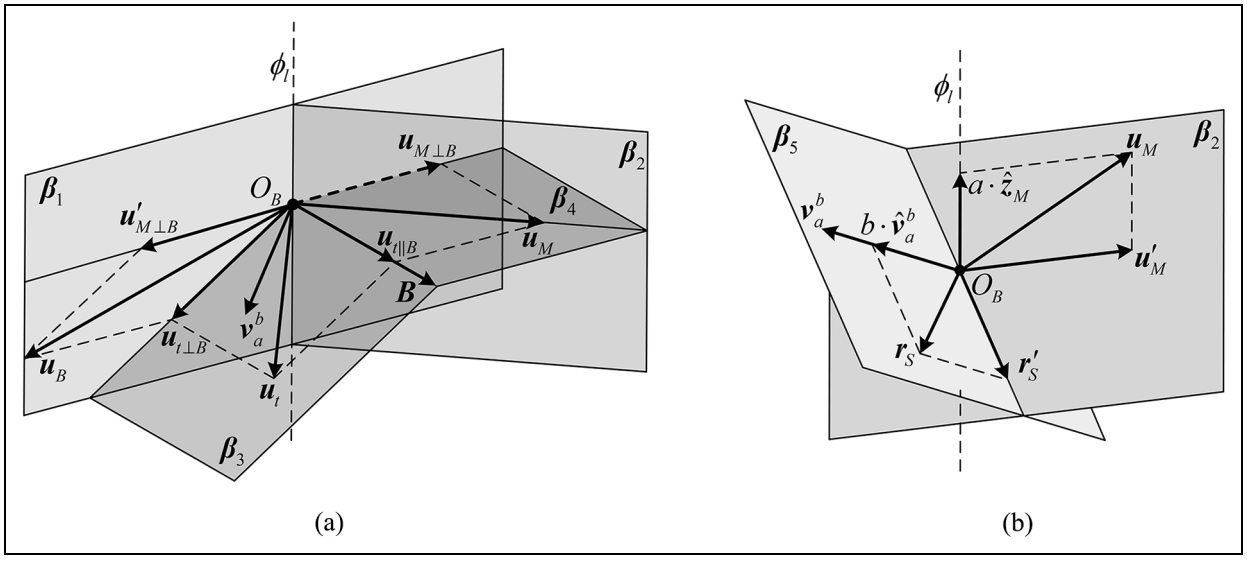

Figure 3. Allocation of the ideal control torque.

where vector $\boldsymbol{u}_{t\|B}$ is parallel to vector $\boldsymbol{B}$, and vector $\boldsymbol{u}_{t\perp B}$ is on plane $\boldsymbol{\beta}_1$.

According to the projection theorem, it yields

$$\boldsymbol{u}_{t\|B} = \hat{\boldsymbol{B}}\left[\left(\hat{\boldsymbol{B}}\right)^{\mathrm{T}}\boldsymbol{u}_t\right] \tag{92}$$

$$\boldsymbol{u}_{t\perp B} = \boldsymbol{u}_t - \boldsymbol{u}_{t\|B} \tag{93}$$

where $\hat{\boldsymbol{B}}$ is the unit vector of $\boldsymbol{B}$.

As the geomagnetic torque $\boldsymbol{u}_B$ is perpendicular to vector $\boldsymbol{B}$, vector $\boldsymbol{u}_{t\|B}$ is the projection of the aerodynamic torque vector $\boldsymbol{u}_M$ in the direction of vector $\boldsymbol{B}$. Vector $\boldsymbol{u}_{M\perp B}$ is the projection of vector $\boldsymbol{u}_M$ on plane $\boldsymbol{\beta}_1$, and its opposite vector is $\boldsymbol{u}'_{M\perp B}$. The sum of vectors $\boldsymbol{u}'_{M\perp B}$ and $\boldsymbol{u}_{t\perp B}$ is the geomagnetic torque $\boldsymbol{u}_B$.

Vector $\boldsymbol{\beta}_4$ is defined as the plane where vector $\boldsymbol{u}_{t\|B}$ and vector $\boldsymbol{u}_M$ lie. If plane $\boldsymbol{\beta}_4$ is perpendicular to plane $\boldsymbol{\beta}_2$, the aerodynamic torque $\boldsymbol{u}'_M$ can be expressed (Chesi et al., 2017) as

$$\boldsymbol{u}'_M = \frac{\boldsymbol{u}_t^{\mathrm{T}}\hat{\boldsymbol{B}}}{\left(\boldsymbol{P}\boldsymbol{u}_{t\|B}\right)^{\mathrm{T}}\hat{\boldsymbol{B}}}\left(\boldsymbol{P}\boldsymbol{u}_{t\|B}\right), \qquad \boldsymbol{P} = \boldsymbol{I}_{3\times 3} - \hat{\boldsymbol{v}}_a^b\left(\hat{\boldsymbol{v}}_a^b\right)^{\mathrm{T}} \tag{94}$$

However, as plane $\boldsymbol{\beta}_4$ and plane $\boldsymbol{\beta}_2$ are not necessarily perpendicular, vector $\boldsymbol{u}_M$ is not unique. To describe vector $\boldsymbol{u}_M$, a unit vector on line ϕ_l is defined as

$$\hat{\boldsymbol{z}}_M = \frac{\boldsymbol{v}_a^b \times \boldsymbol{B}^b}{\left\|\boldsymbol{v}_a^b \times \boldsymbol{B}^b\right\|} \tag{95}$$

Thus, the aerodynamic torque $\boldsymbol{u}_M$ and the geomagnetic torque $\boldsymbol{u}_B$ can be expressed as

$$\boldsymbol{u}_M = \boldsymbol{u}'_M + a \cdot \hat{\boldsymbol{z}}_M, \qquad \boldsymbol{u}_B = \boldsymbol{u}_t - \boldsymbol{u}_M \tag{96}$$

where the coefficient $a \in \boldsymbol{R}$.

Another plane $\boldsymbol{\beta}_5$, which is perpendicular to the vector $\boldsymbol{u}_M$, is defined. The CoM position vector is given by

$$\boldsymbol{r}_s = \boldsymbol{r}'_s + b \cdot \hat{\boldsymbol{v}}_a^b, \qquad \boldsymbol{r}'_s = -\frac{\boldsymbol{F}_{aero} \times \boldsymbol{u}_M}{\|\boldsymbol{F}_{aero}\|^2} \tag{97}$$

where the coefficient $b \in \boldsymbol{R}$.

Assume that three straight lines, on which three moving masses move along, are parallel to three axes of the $O_B X_B Y_B Z_B$ system. The moving mass position vector $\boldsymbol{L} = [l_1, l_2, l_3]^{\mathrm{T}}$ and the magnetic moment vector $\boldsymbol{m}_B = [m_{B1}, m_{B2}, m_{B3}]^{\mathrm{T}}$ are

$$\begin{aligned} \boldsymbol{L} &= (M + m_1 + m_2 + m_3)\mathrm{diag}\left(\frac{1}{m_1}, \frac{1}{m_2}, \frac{1}{m_3}\right)\boldsymbol{r}_s, \\ \boldsymbol{m}_B &= \frac{\boldsymbol{B} \times \boldsymbol{u}_B}{\|\boldsymbol{B}\|^2} \end{aligned} \tag{98}$$

Remark 4: Due to the existence of coefficients a and b in the expression of vector $\boldsymbol{r}_s$, the result of control allocation is uncertain. By choosing the proper coefficients, the motion of the moving masses can be optimized to reduce the additional torque. This optimization problem can be solved via a traditional nonlinear optimization algorithm or intelligent algorithm.

Remark 5: From (94), it can be seen that the smaller the angle between vectors $\boldsymbol{v}_a^b$ and $\boldsymbol{B}$, the larger the aerodynamic torque $\boldsymbol{u}_M$ tends to be. This could lead to the frequent and severe overshooting of two actuators, and thus the constraints on two actuators are particularly necessary. The system will even degenerate into an underactuated system when the relative flow vector is parallel to the geomagnetic field vector.

Simulation results

In this section, the developed control scheme is applied to a LEO 3U CubeSat to demonstrate its effectiveness. The prototype of the moving mass actuator presented in section 1 is used for semi-physical simulation, and its power is about 1.35 W. The energy consumption of this linear motor is related to the acceleration of the mass. The acceleration is strictly limited by the backstepping controller to reduce the additional disturbance. To further optimize the energy consumption, this linear motor can be replaced to avoid a steady-state current for positioning, such as by the non-captive stepper motor with a self-locking function proposed in the work by Polat (2016). In addition, a lighter mass can reduce the working current, but will lead to a reduction in the aerodynamic control torque.

As shown in Figure 4, the semi-physical simulation platform was built for two actuators. The attitude dynamics and kinematics were conducted in the MATLAB/Simulink environment in the simulation computer, and the control laws were calculated in the C environment in the ADCS CPU. Notably, three moving masses were all placed on the horizontal plane to eliminate the influence of gravity. It can be seen that the three-axis magnetorquer includes one air-core coil and two iron-core coils.

As shown in the flow diagram of the semi-physical simulation process in Fig. 5, the closed-loop system was constructed by an ADCS CPU, two actuators, a data collection system, and a simulation computer. The two actuators were fully physically accessible, and their feedback information was collected through the data collection system. The attitude information was updated in the simulation computer and then sent to the ADCS CPU to calculate the control laws.

The International Geomagnetic Reference Field (IGRF-12) model was used to provide the geomagnetic field information, and the ideal aerodynamic model was used to provide the aerodynamic force (Chesi et al., 2017). A Runge-Kutta algorithm was used for the iteration of attitude dynamics and kinematics, and the step size was set to 200 ms.

Accordingly, the position vectors of three moving masses are, respectively, given by $\boldsymbol{p}_1 = [l_1, 0.01, -0.01]^{\mathrm{T}}$, $\boldsymbol{p}_2 = [-0.01, l_2, 0.01]^{\mathrm{T}}$, and $\boldsymbol{p}_3 = [0.01, -0.01, l_3]^{\mathrm{T}}$. The size of the CubeSat is 110 mm $\times$ 110 mm $\times$ 320 mm, and the corresponding aerodynamic properties can be derived from the prototype design. The parameters of the satellite and proposed control scheme are listed in Tables 1 and 2, respectively. For this particular design, the position of the system CoM can be adjusted within $\pm$1.35 mm to modulate the aerodynamic torque direction and magnitude.

As presented in Figures 6–7, four different cases were employed for comparison to elaborate the performance of the

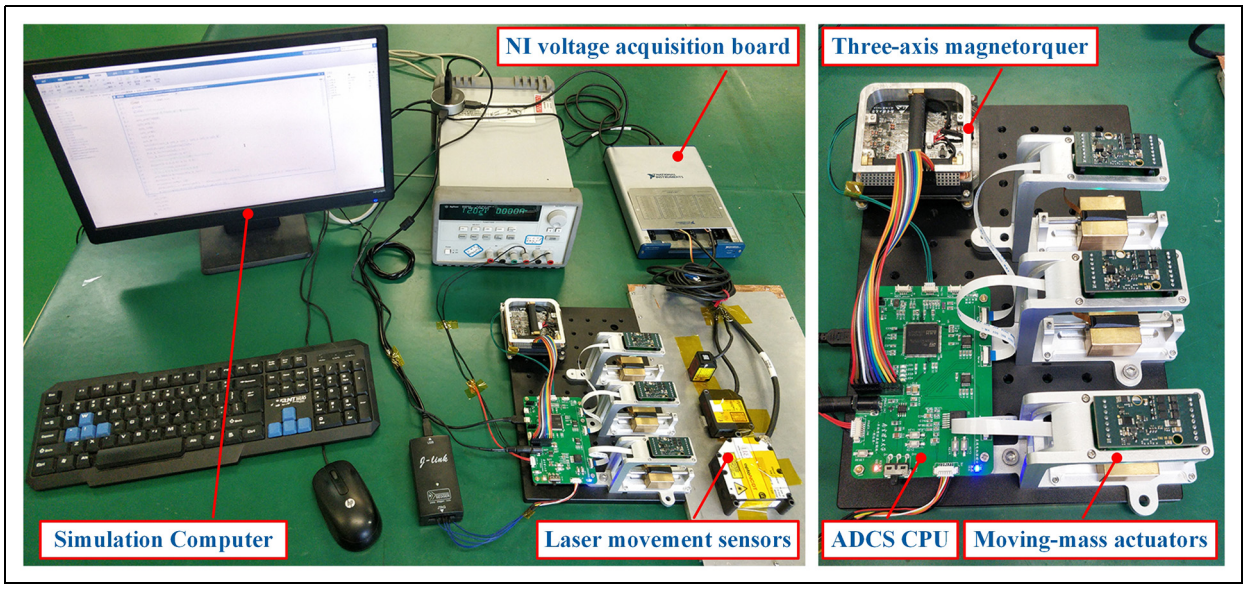

Figure 4. Semi-physical simulation platform for two actuators.

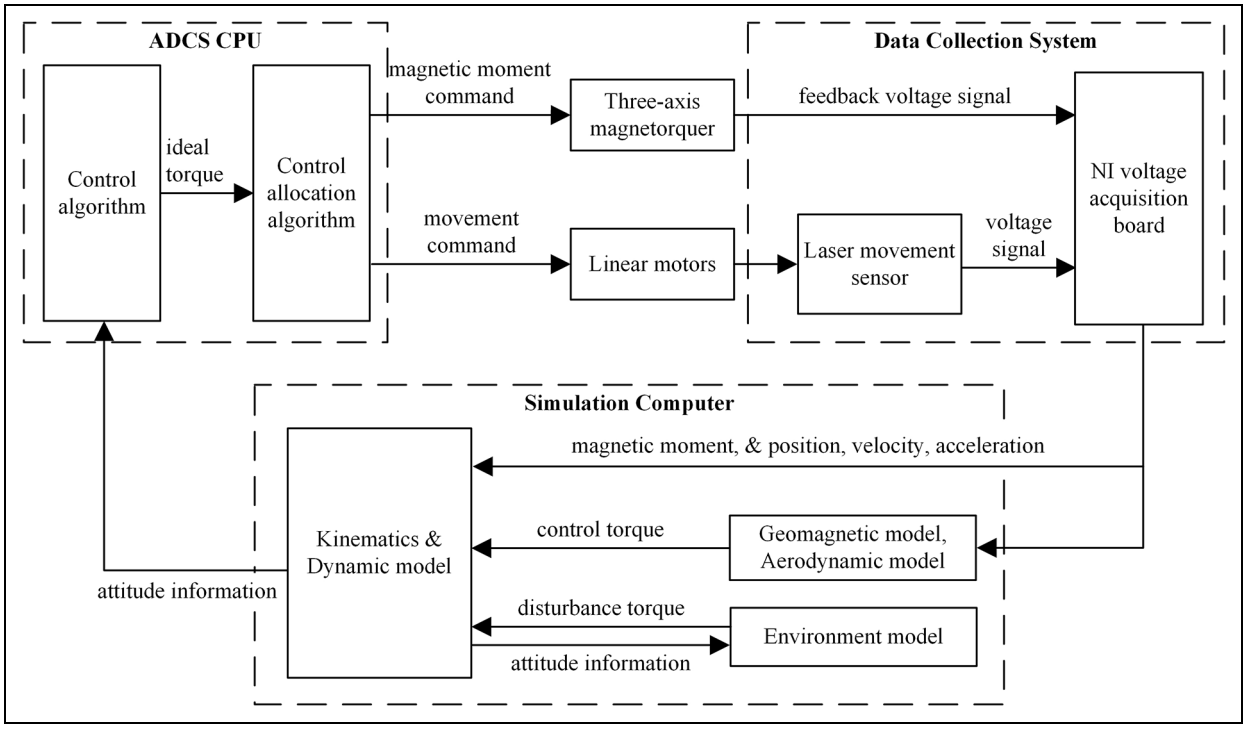

Figure 5. The flow diagram of the semi-physical simulation process.

proposed control scheme. The designed controller presented in this paper is adopted in Case 1. Compared with the controller designed in this paper, the convergence parameter k is not adaptive in Cases 2 and 3, presented in the work by Zhou et al. (2017). The parameter k is chosen to be 0.02 in Case 2 and 0.06 in Case 3. In Case 4, the robust controller without a disturbance observer presented in the study by Zou et al. (2016) is introduced for comparison, where k is adaptive.

As expected, the plot of error attitude shows that, in less than 800 s, the designed controller can drive the error MRS to converge to a small bounded region within 10^{-4} despite the existence of parametric uncertainties, external disturbance, and control input constraints. In Case 2, before 150s,

Table 1. Parameters of CubeSat.

Parameter	Simulation value
Mass	$M = 1531$ g, $m_1 = m_2 = m_3 = 146$ g
Moment of inertia	$\boldsymbol{J}_B = \text{diag}(0.004, 0.008, 0.008)$ kg · m^2
Limitation of masses position	± 0.018 m
Limitation of magnetic moment	± 0.05 A · m^2
Coefficient of aerodynamic force (Chesi, 2015)	$0.5\rho\|\|\boldsymbol{v}_a^b\|\|^2 C_D = 0.0018$
Disturbances	$\Delta\boldsymbol{r}_s = [0.002, -0.001, 0.001]^{\mathrm{T}}$ m $\Delta\boldsymbol{F}_{aero} = [0.25\cos(\pi t/2700) + 0.05]\boldsymbol{F}_{aero}$ $\Delta\boldsymbol{m}_B = [0.005, 0.004, -0.003]^{\mathrm{T}}$ A · m^2 $\Delta\boldsymbol{d} = [5, -5, -8]^{\mathrm{T}} \times 10^{-8}$ N · m
Parameters of orbit	orbit height: $h = 350$ km orbit inclination: $i = 96.6765^\circ$ orbit period: $T_0 = 5492.1$ s

because the adaptive parameter k in Case 1 is close to its minimum value of 0.02, the time responses of angular velocity in Cases 1 and 2 are similar. However, after 150 s, the angular velocity in Case 1 gradually becomes greater than that in Case 2, and thus a higher convergence speed is obtained. It can be seen from Figure 6 that it takes more than 1200 s to reach the target attitude in Case 2. On the contrary, in Case 3, the controller exhibits poorer performance due to its excessive fluctuation of the angular velocity, which will lead to the large overshoot of actuators. In Case 4, there exists no compensation for disturbances. The lack of disturbance rejection ability is the deficiency of the controller in Case 4, which leads to an obvious deviation of the error MRS.

Notably, as shown in Figure 8, along with the attitude error approaching zero, the adaptive parameter k converges from its lower bound of 0.02 to its upper bound of 0.06. Thus, the designed controller exhibits better performance with a smoother trend of attitude change before 300 s, and a higher convergence speed after 300 s. Therefore, the designed speed-adaptive control scheme has a better attitude control performance compared with those generated by the pure dynamic surface approach and the robust approach in the presence of various disturbances.

As shown in Figures 9(c–d), the magnitudes of the actual control torque, its first derivative, and its second derivative always remain within their respective constrained regions. It can also be seen in Figure 9(a) that the curves of the actual control torque present a smooth and slow trend. The existence of hard constraints on the two actuators yields a difference between the actual control torque and the ideal control torque, which is the control error shown in Figure 9(b).

Figure 10 shows the time response of the nonlinear disturbance observer. There exists a large peak of the disturbance before 150 s due to the large control error. The rapid change in the control error leads to an obvious error between the actual disturbance and the observed disturbance when 60 s <

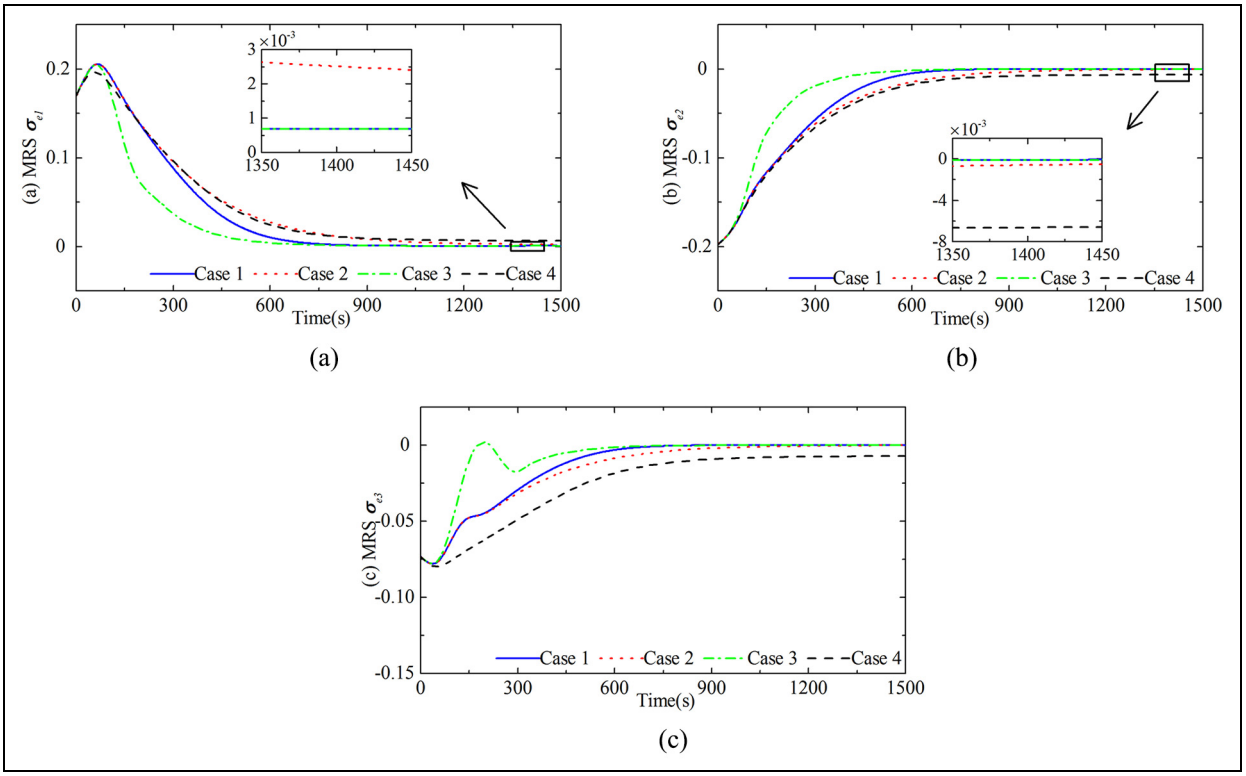

Figure 6. Comparison of the time responses of the error MRS in four cases.

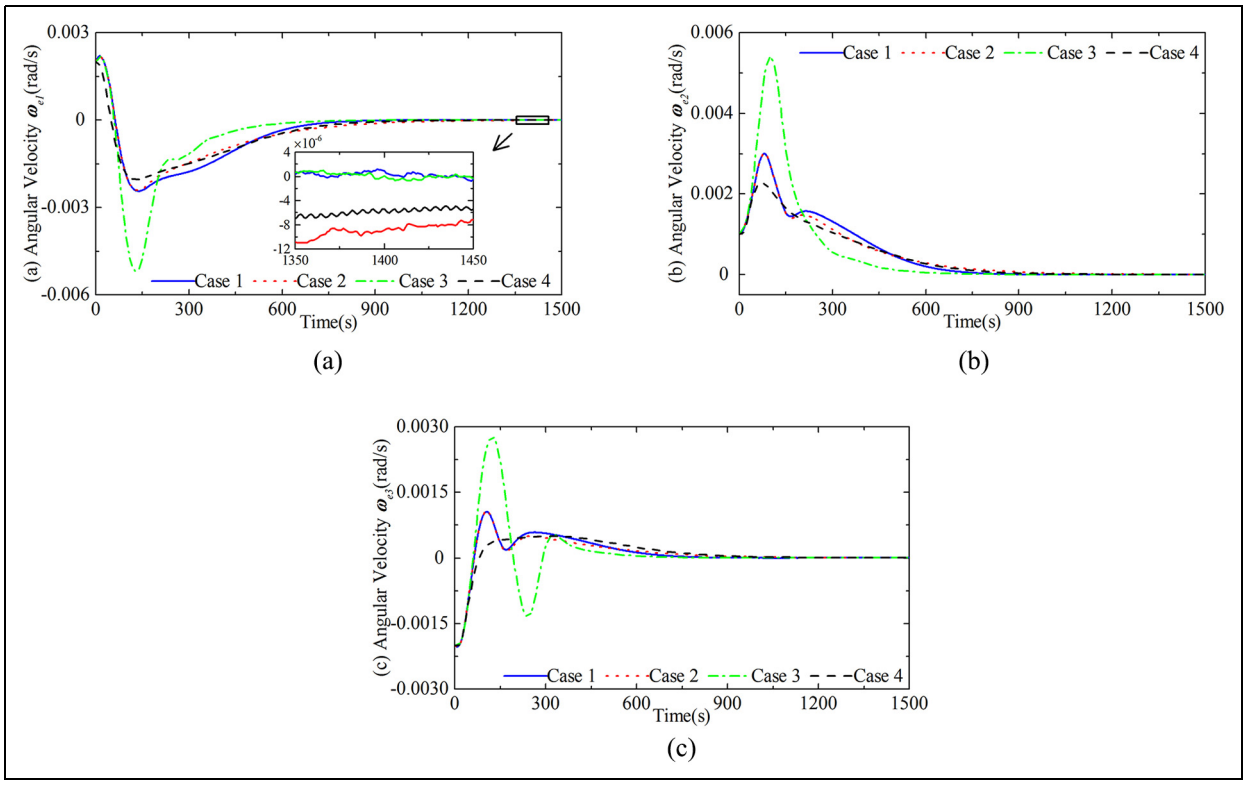

Figure 7. Comparison of the time responses of the error angular velocity in four cases.

Table 2. Parameters of the controller.

Parameter	Simulation value
Initial attitude	$\sigma_{bo0} = [0.15, -0.05, 0.05]^T$ $\omega_{bo0} = [0.003, 0.005, -0.006]^T$ rad/s
Desired attitude	$\sigma_{bod} = [-0.05, 0.1, 0.15]^T$ $\omega_{bod} = [0, 0, 0]^T$ rad/s
Parameters of observer	$\lambda_1 = \lambda_2 = \lambda_3 = 5$, $s_1 = s_2 = s_3 = 3$, $\hat{\mathbf{d}}_0 = [0, 0, 0]^T$
Parameters of first adaptive law	$\gamma_1 = 0.01$, $\varepsilon_1 = 5\times10^{-7}$, $k_u = 0.06$ $k_l = 0.02$, $k_0 = 0.02$
Parameters of second adaptive law	$\gamma_2 = 1$, $\varepsilon_2 = [1, 1, 1]^T\times10^{-8}$, $\hat{\mathbf{d}}_0^+ = [1, 1, 1]^T\times10^{-7}$
The auxiliary control signals	$\boldsymbol{v}_0 = [0, 0, 0]^T$, $\boldsymbol{w}_0 = [0, 0, 0]^T$, $\boldsymbol{q}_0 = [0, 0, 0]^T$
Parameters of input constraints	$\boldsymbol{u}_M = [1, 1, 1]^T\times10^{-6}$, $\boldsymbol{v}_M = [1, 1, 1]^T\times10^{-8}$ $\boldsymbol{w}_M = [5, 5, 5]^T\times10^{-9}$
Coefficients of controller	$\mathbf{c}_e = \text{diag}(8, 15, 8)\times10^{-6}$, $c_1 = 0.05$, $c_2 = c_3 = c_4 = 2.5$
Coefficients of filters	$\tau_2 = \tau_3 = \tau_4 = 0.2$
Coefficients of control allocation	$a = b = 0$

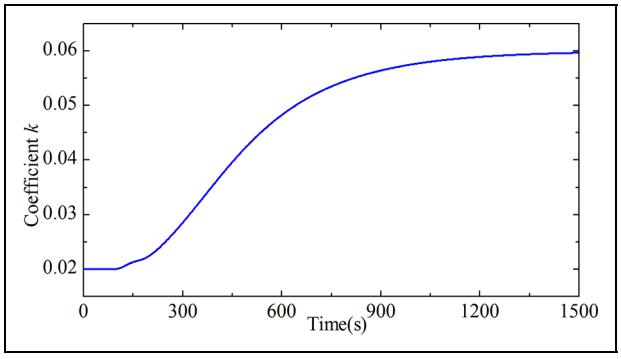

Figure 8. Time response of the parameter k in Case 1.

$t < 100$ s. By appropriately reducing the value of $\boldsymbol{v}_M$, the observer could better track the disturbance. When $t \geqslant 200$ s, the observer error converges to less than $\pm1\times10^{-5}$. Thus, the nonlinear observer is capable of simultaneously achieving the precise estimation of model uncertainties, control errors, and other slow-varying disturbances. The effects of the disturbances on attitude control are minimized by the nonlinear disturbance observer through feedforward compensation.

Figures 11–12 present actual inputs of the two actuators. It can be seen that, from 30s to 125s, the y-axis and z-axis mass positions are strictly limited within ±0.018 m by the smooth

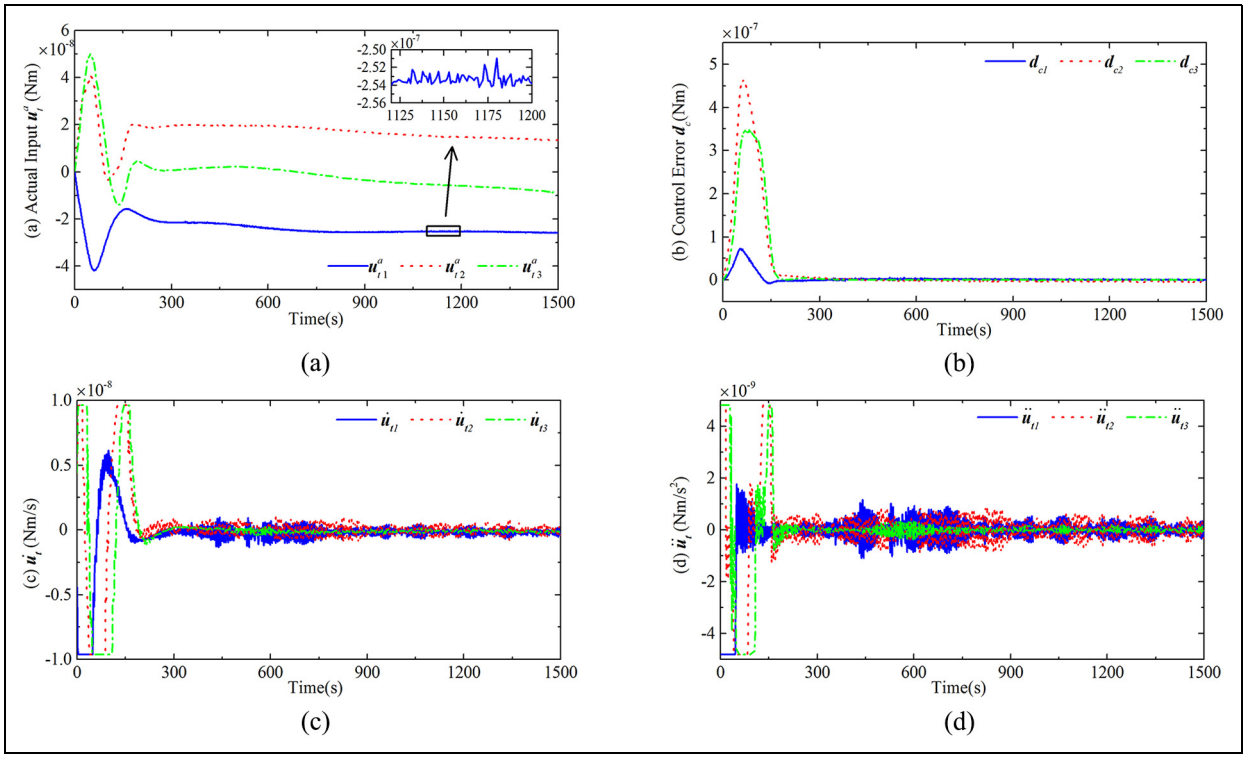

Figure 9. Control input in Case 1. (a) Three- dimensional actual torque input. (b) Control errors. (c) First derivative of control input. (d) Second derivative of control input.

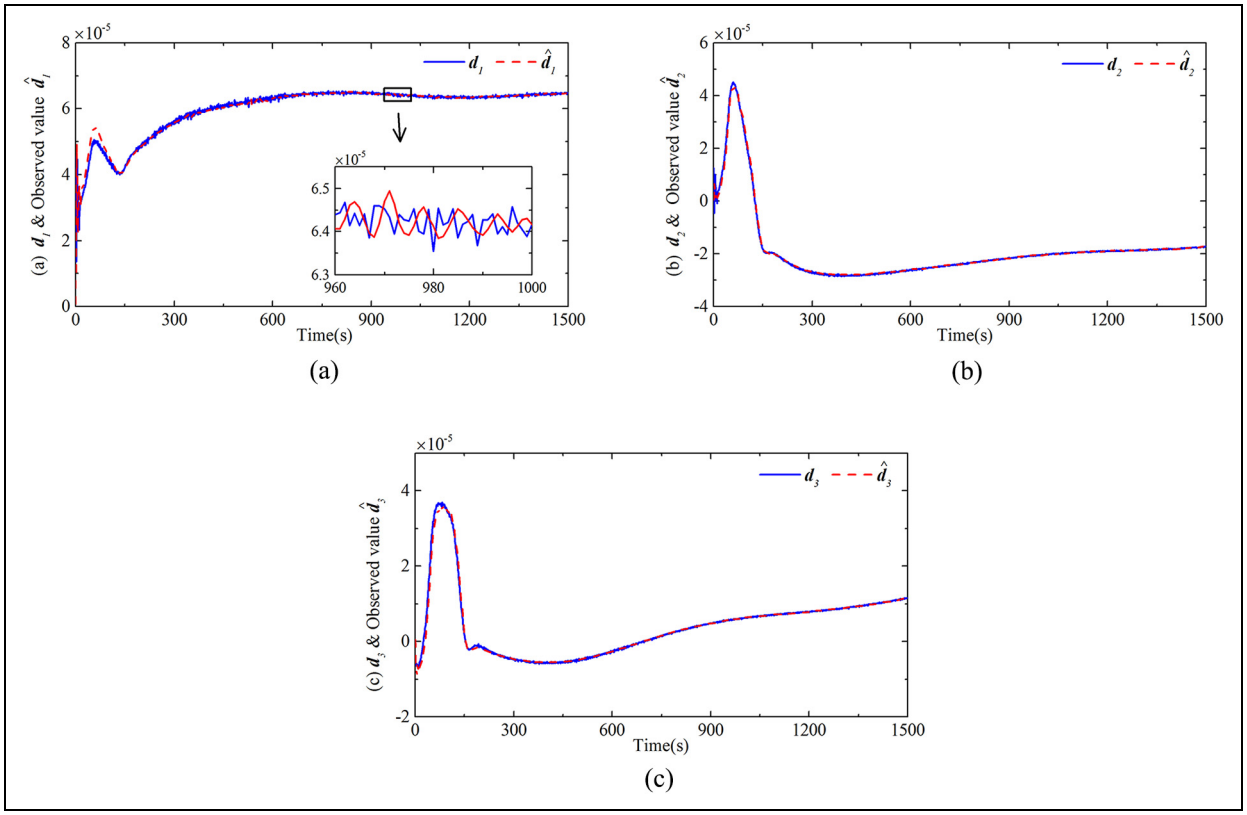

Figure 10. Estimation of the system disturbance in Case 1.

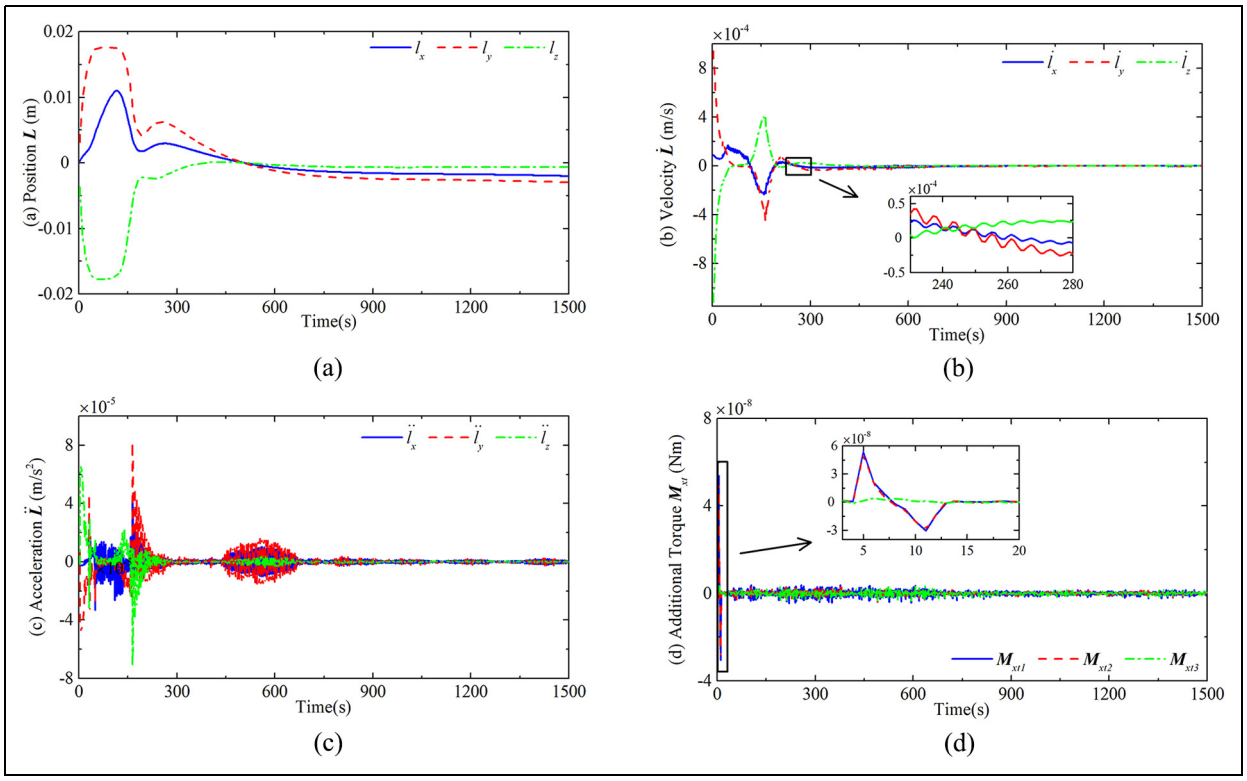

Figure 11. Movement of moving masses based on tanh(■) in Case 1.
(a) Position. (b) Velocity. (c) Acceleration. (d) Additional torque.

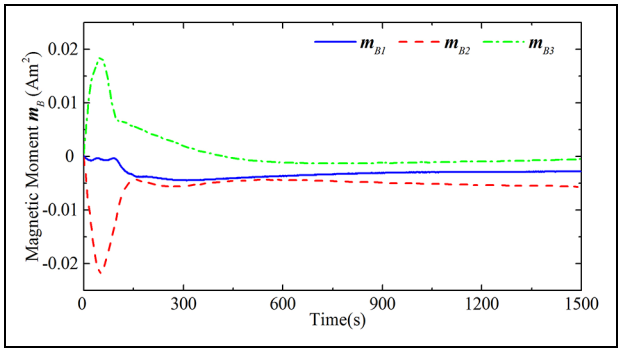

Figure 12. Actual magnetic moment signal in Case 1.

hyperbolic tangent function. Although hard constraints are imposed on the two actuators at certain moments, the steady controlling performance presented in Figure 6 illustrates the effectiveness of the designed controller. In particular, to compensate for the system disturbances, neither of the control inputs of the two actuators converge to their origins. Figure 11(a) shows that when the masses barely move in the final attitude, the additional torque will approach zero, which enables higher pointing accuracy for a LEO nanosatellite.

For comparison, the sign function was used to constrain the inputs of two actuators in the simulation, as presented in Figure 13. It can be seen from Figure 13(a) that the sudden change of the position signals at the starting and ending moments of saturation yields an instantaneous surge of acceleration and additional torque. This means that the position saturation will introduce violent attitude jitter. Instead, as presented in Figure 11(d), due to the use of the smooth hyperbolic tangent function and the multiple constraints on the control input, the fast-varying disturbance was reduced to $\pm 6 \times 10^{-8}$. It can be neglected as compared with other slow-varying disturbances.

Conclusion

In this paper, a method of using a set of moving masses and a three-axis magnetorquer to achieve attitude maneuver was presented. A speed-adaptive dynamic surface control scheme was proposed to comprehensively solve the practical problems of aerodynamic model error, the dynamic effect of movement, stroke limitation, and slow convergence. The dynamic effect of the movement, which is the fast-varying disturbance, is reduced to be negligible by imposing the multiple constraints on the input magnitude, its first derivative, and its second derivative. Other unknown disturbances are considered to be slow-varying and are precisely estimated by a nonlinear observer. Due to the designed speed-adaptive law, the overshoot of two actuators is small when the attitude error is large, and the attitude convergence speed is large when the attitude error is small. By using the Lyapunov approach, it is proven that, despite uncertain dynamics, unknown disturbance, and input

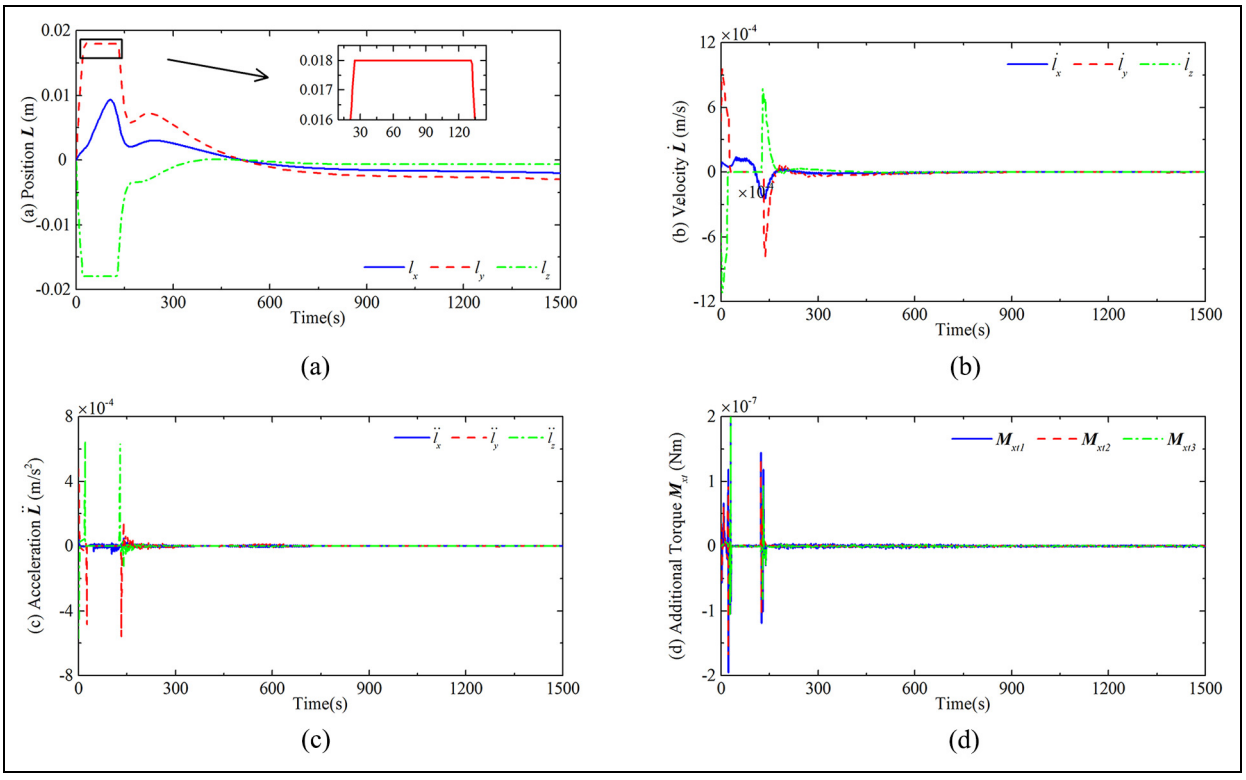

Figure 13. Movement of moving masses based on sign(·) for comparison. (a) Position. (b) Velocity. (c) Acceleration. (d) Additional torque.

constraints, the attitude error can be adjusted to be arbitrarily small by choosing the proper parameters. A semi-physical simulation platform was built to verify the feasibility of the moving mass actuator and the effectiveness and robustness of the designed controller. However, the semi-physical simulation platform that was used to examine the control performance was only built for two actuators. Future works will be devoted to semi-physical simulation with actual attitude measuring sensors to further promote practical application.

Declaration of conflicting interests

The author(s) declared no potential conflicts of interest with respect to the research, authorship, and/or publication of this article.

Funding

The author(s) disclosed receipt of the following financial support for the research, authorship, and/or publication of this article: This work was supported in part by the National Natural Science Foundation of China under Grant 61803204, and in part by the Natural Science Foundation of Jiangsu Province under Grant BK20180465.

ORCID iDs

Yuandong Hu https://orcid.org/0000-0002-1495-2876
Zhengliang Lu https://orcid.org/0000-0003-1856-5950
Wenhe Liao https://orcid.org/0000-0002-1710-4311

References

Akella MR, Valdivia A and Kotamraju GR (2005) Velocity-free attitude controllers subject to actuator magnitude and rate saturations. *Journal of Guidance, Control, and Dynamics* 28(4): 659–666.

Atkins BM and Henderson TA (2012) Under-actuated moving mass attitude control for a 3U cubesat mission. In: *Proceedings of the 22nd AAS/AIAA Space Flight Mechanics Meeting*, Charleston, South Carolina, 29 January–2 February 2012, pp. 2083–2094. San Diego, California: Univelt.

Butt WA, Yan L and Kendrick AS (2013) Adaptive dynamic surface control of a hypersonic flight vehicle with improved tracking. *Asian Journal of Control* 15(2): 594–605

Butt WA, Yan L and Kendrick AS (2015) Adaptive integral dynamic surface control of a hypersonic flight vehicle. *International Journal of Systems Science* 46(10): 1717–1728.

Chen WH, Ballance DJ, Gawthrop PJ, et al. (2000) A nonlinear disturbance observer for robotic manipulators. *IEEE Transactions on Industrial Electronics* 47(4): 932–938

Chesi S (2015) Attitude control of nanosatellites using shifting masses. PhD Thesis, University of California, USA.

Chesi S, Gong Q, Pellegrini V, et al. (2014) Automatic mass balancing of a spacecraft three-axis simulator: analysis and experimentation. *Journal of Guidance, Control, and Dynamics* 37(1): 197–206.

Chesi S, Gong Q and Romano M (2017) Aerodynamic three-axis attitude stabilization of a spacecraft by center-of-mass shifting. *Journal of Guidance, Control, and Dynamics* 40(7): 1613–1626.

Childs DW (1971) A movable-mass attitude-stabilization system for artificial-g space stations. *Journal of Spacecraft and Rockets* 8(8): 829–834.

Edwards TL and Kaplan MH (1974) Automatic spacecraft detumbling by internal mass motion. *AIAA Journal* 12(4): 496–502.

Firuzi S and Gong S (2018) Attitude control of a flexible solar sail in low Earth orbit. *Journal of Guidance, Control, and Dynamics* 41(8): 1715–1730.

Gao S, Ning B and Dong H (2016) Fuzzy dynamic surface control for uncertain nonlinear systems under input saturation via truncated adaptation approach. *Fuzzy Sets and Systems* 290(1): 100–117.

Guo PF and Zhao LY (2013) Modeling and attitude control of a spinning spacecraft with internal moving mass. *Advanced Materials Research* 760–762(1): 1216–1220.

Hill DE (2017) Dynamics and control of spinning spacecraft using translating masses with friction compensation. *Journal of Spacecraft and Rockets* 54(6): 1376–1382.

Ioannou PA and Sun J (1995) *Robust Adaptive Control*. PTR: Prentice-Hall, Inc.

Kumar K and Zou A (2010) Attitude control of miniature satellites using movable masses. In: *Ryerson University SpaceOps 2010 Conference, 25–30 April 2010*, Huntsville, Alabama, USA, pp. 1–6.

Lovera M, Marchi ED and Bittanti S (2002) Periodic attitude control techniques for small satellites with magnetic actuators. *IEEE Transactions on Control Systems Technology* 10(1): 90–95.

Lu Z (2017) Study on mass moment attitude control for fast orbit maneuver satellite. PhD Thesis, Nanjing University of Science and Technology, China.

Lu Z and Zhang X (2016) Mass moment attitude control system design for nano-satellite in orbital transition. *Acta Aeronautica et Astrinautica Sinica* 38(6): 1–10.

Luo W, Chu Y-C and Ling K-V (2005) H-infinity inverse optimal attitude-tracking control of rigid spacecraft. *Journal of Guidance, Control, and Dynamics* 28(3): 481–494.

Menon PK, Sweriduk GD, Ohlmeyer EJ, et al. (2004) Integrated guidance and control of moving-mass actuated kinetic warheads. *Journal of Guidance, Control, and Dynamics* 27(1): 118–126

Petsopoulos T, Regan FJ and Barlow J (1996) Moving-mass roll control system for fixed-trim re-entry vehicle. *Journal of Spacecraft and Rockets* 33(1): 54–60

Polat HC (2016) Prototype design and mission analysis for a small satellite exploring environmental disturbances for attitude stabilization. PhD Thesis, Naval Postgraduate School, USA.

Polycarpou MM and Ioannou PA (1993) A robust adaptive nonlinear control design. In: *1993 American Control Conference*, San Francisco, CA, USA, 2–4 Jun 1993, pp. 423–427.

Psiaki ML (2004) Nanosatellite attitude stabilization using passive aerodynamics and active magnetic torquing. *Journal of Guidance, Control, and Dynamics* 27(3): 347–355.

Swaroop D, Hedrick JK, Yip PP, et al. (2000) Dynamic surface control for a class of nonlinear systems. *IEEE Transactions on Automatic Control* 45(10): 1893–1899.

Virgili-Llop J, Polat HC and Romano M (2016) Using shifting masses to reject aerodynamic perturbations and to maintain a stable attitude in very low Earth orbit. In: *26th AAS/AIAA Space Flight Mechanics Meeting*, Napa, CA, USA, pp. 2129–2148.

Virgili-Llop J, Polat HC and Romano M (2019) Attitude stabilization of spacecraft in very low Earth orbit by center-of-mass shifting. *Frontiers in Robotics and AI* 6(7): 1–19.

Wang D and Jie H (2005) Neural network-based adaptive dynamic surface control for a class of uncertain nonlinear systems in strict-feedback form. *IEEE Transactions on Neural Networks* 16(1): 195–202.

Wang Z and Wu Z (2015) Nonlinear attitude control scheme with disturbance observer for flexible spacecrafts. *Nonlinear Dynamics* 81(1): 257–264.

Wie B and Murphy D (2007) Solar-sail attitude control design for a flight validation mission. *Journal of Spacecraft and Rockets* 44(4): 809–821.

Xia G, Sun C, Zhao B, et al. (2019) Neuroadaptive distributed output feedback tracking control for multiple marine surface vessels with input and output constraints. *IEEE Access* 7(1): 123076–123085.

Xia Y, Zhu Z, Fu M, et al. (2011) Attitude tracking of rigid spacecraft with bounded disturbances. *IEEE Transactions on Industrial Electronics* 58(2): 647–659.

Ye D, Zhang X, Wan X, et al. (2018) Finite time control strategy for satellite attitude maneuver based on hybrid actuator. *Transactions of the Institute of Measurement and Control* 40(9): 2798–2806.

Yu C and Xie X (2019) Dynamic sliding mode-based attitude stabilisation control of satellites with angular velocity and control constraints. *Transactions of the Institute of Measurement and Control* 41(4): 934–941.

Zhang X, Zhang X, Lu Z, et al. (2019) Optimal path planning-based finite-time control for agile CubeSat attitude maneuver. *IEEE Access* 7(1): 102186–102198.

Zhou C, Zhu J, Lei H, et al. (2017) Observer-based dynamic surface control for high-performance aircraft subjected to unsteady aerodynamics and actuator saturation. *Proceedings of the Institution of Mechanical Engineers, Part I: Journal of Systems and Control Engineering* 231(6): 481–494

Zou AM, Kumar KD and de Ruiter AHJ (2016) Robust attitude tracking control of spacecraft under control input magnitude and rate saturations. *International Journal of Robust and Nonlinear Control* 26(4): 799–815

Zou AM, Kumar KD, Hou Z, et al. (2011) Finite-time attitude tracking control for spacecraft using terminal sliding mode and chebyshev neural network. *IEEE Transactions on Systems, Man, and Cybernetics, Part B (Cybernetics)* 41(4): 950–963.